

# Design optimization of tensile-strained SiGeSn/GeSn quantum wells at room temperature

Cite as: J. Appl. Phys. **129**, 123102 (2021); <https://doi.org/10.1063/5.0042482>

Submitted: 30 December 2020 . Accepted: 03 March 2021 . Published Online: 22 March 2021

 Z. Chen,  Z. Ikonic,  D. Indjin, and  R. W. Kelsall



View Online



Export Citation



CrossMark

## ARTICLES YOU MAY BE INTERESTED IN

[Submonolayer quantum dot quantum cascade long-wave infrared photodetector grown on Ge substrate](#)

Applied Physics Letters **118**, 081102 (2021); <https://doi.org/10.1063/5.0038844>

[Monolithic infrared silicon photonics: The rise of \(Si\)GeSn semiconductors](#)

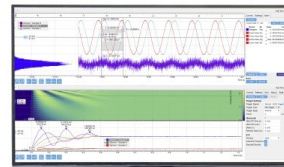
Applied Physics Letters **118**, 110502 (2021); <https://doi.org/10.1063/5.0043511>

[Imaging confined and bulk p-type/n-type carriers in \(Al,Ga\)N heterostructures with multiple quantum wells](#)

Applied Physics Letters **118**, 032104 (2021); <https://doi.org/10.1063/5.0026826>

Challenge us.

What are your needs for periodic signal detection?



Zurich  
Instruments

# Design optimization of tensile-strained SiGeSn/GeSn quantum wells at room temperature

Cite as: J. Appl. Phys. 129, 123102 (2021); doi: 10.1063/5.0042482

Submitted: 30 December 2020 · Accepted: 3 March 2021 ·

Published Online: 22 March 2021



View Online



Export Citation



CrossMark

Z. Chen,<sup>a)</sup> Z. Ikonc,<sup>a)</sup> D. Indjin,<sup>a)</sup> and R. W. Kelsall<sup>a)</sup>

## AFFILIATIONS

School of Electronic and Electrical Engineering, University of Leeds, LS2 9JT Leeds, United Kingdom

<sup>a)</sup>Authors to whom correspondence should be addressed: [chenzhichao1994@hotmail.com](mailto:chenzhichao1994@hotmail.com); [Z.Ikonc@leeds.ac.uk](mailto:Z.Ikonc@leeds.ac.uk); [D.Indjin@leeds.ac.uk](mailto:D.Indjin@leeds.ac.uk); and [R.W.Kelsall@leeds.ac.uk](mailto:R.W.Kelsall@leeds.ac.uk)

## ABSTRACT

A direct bandgap can be engineered in Ge-rich group-IV alloys by increasing Sn content and by introducing tensile strain in GeSn. Here, we combine these two routes in quantum well (QW) structures and systematically analyze the properties of SiGeSn/GeSn quantum wells for a range of Sn content, strain, and well width values, within realistic boundaries. Using the  $\mathbf{k} \cdot \mathbf{p}$  method, and including L-valley within the effective mass method, we find that 13–16 nm is a preferred range of well widths to achieve high gain for tensile-strained SiGeSn/GeSn quantum wells. Within the range of the well widths, a loss ridge caused by inter-valence band absorption and free carrier absorption is found in the region of parameter space where Sn content and strain in the well are related as  $\text{Sn}(\%) \approx -7.71\epsilon_{xx}(\%) + 17.13$ . Limited by a practical strain boundary of 1.7%, for a 14 nm quantum well, we find that  $7.5 \pm 1\%$  Sn and  $1 \pm 0.2\%$  strain is a promising combination to get a good net gain for photon transition energy higher than  $\sim 0.42$  eV. A maximum utilization of strain is preferred to obtain the best gain with lower energies ( $< 0.42$  eV). By comparing these designs with a compressive strain example, an engineered tensile structure shows a better performance, with a low threshold current density ( $1.42$  kA/cm<sup>2</sup>). Finally, the potential benefit of p-doping of the tensile-strained GeSn QW is also discussed.

Published under license by AIP Publishing. <https://doi.org/10.1063/5.0042482>

## I. INTRODUCTION

Conventional group-IV materials Si and Ge are inadequate as efficient light emitters because of their indirect bandgap. This can be overcome by adding a sufficiently large Sn content. The Sn content in the GeSn alloy should exceed 6.5% for it to be a direct bandgap material,<sup>1,2</sup> but for an efficient laser, the Sn content should be much larger than that. The first working GeSn laser was demonstrated in 2015,<sup>3</sup> but it operated only up to 90 K. The operation temperature was later increased to 230 K by using higher Sn content in the active layer<sup>4</sup> (16%). These lasers are both optically pumped. A big step toward realization of an electric pumped laser with high Sn content was achieved recently.<sup>5</sup> Using Ge<sub>0.89</sub>Sn<sub>0.11</sub> as the active region, lasing operation up to 100 K was observed.

The high Sn content converting GeSn into a direct bandgap semiconductor also has its downsides. A high defect density will appear due to the large lattice mismatch between Ge and Sn. Defects act as electron and hole recombination and trapping centers and prevent the higher temperature operation of such lasers. Introducing tensile strain is another way to make the bandgap more “direct.” Using the data for the deformation

potential (DP) of the  $\Gamma$  and L valleys in Refs. 6 and 7, pure Ge will become direct under a biaxial strain of 1.79%. If used together with alloying Sn and Ge, this may deliver a defect-free direct bandgap material, hence a better lasing performance can be expected. This trend has been proved in Ref. 8, where an ultra-low threshold laser was realized by using alloys with only 5.4% Sn, with tensile strain introduced by SiN<sub>x</sub> in the active region.

Experience from the development of mature group III-V based lasers indicates that a big improvement of the laser performance can be achieved by using quantum size effects. The SiGeSn/GeSn QWs were grown and characterized by many experimentalists, indicating it is a promising light emitting material.<sup>9–13</sup> A much lower threshold for SiGeSn/GeSn multi-quantum-well (MQW) than bulk was justified in Ref. 14, showing that an MQW structure is a more efficient choice than bulk for the laser active region. Instead of using Ge or GeSn as a barrier (buffer) layer,<sup>15,16</sup> SiGeSn is more preferable barrier material,<sup>13</sup> because it enables a deeper well and allows independent engineering of the band alignment and lattice constant (this gives more room for the choice of strain in the well). Also, according to the results from Refs. 17 and 18,

MQW has a larger optical confinement factor compared with SQW, and by carefully choosing the number of QWs, an optimal performance can be reached.

The modeling of GeSn QWs has often been carried out in parallel with the experimental work. The  $\mathbf{k} \cdot \mathbf{p}$  method was usually employed to calculate the band structure of tensile or compressive strained QW.<sup>19–21</sup> The importance of L-valley has also been addressed in these studies, as it is much closer to the  $\Gamma$ -valley compared to the conventional III-V structures. However, this research was mainly focused on engineering the Sn content based on a specific design, while the possible improvements coming from tensile strain were not thoroughly studied. Later, Liu *et al.*<sup>22</sup> proposed a tensile-strained MQW device wrapped in SiN stressor, and the calculations indicated a better performance of tensile-strained QW than of a relaxed device. Inter-valence band absorption (IVBA) has been studied for bulk material,<sup>23</sup> but it was seldom mentioned in QW modeling. In this work, in order to explore the optimum design of GeSn/SiGeSn MQW based laser structures, instead of considering a specific structure, we consider Sn content and strain as independent variables. After specifying the appropriate well width, we look into the parameter space of Sn content and strain and do the gain calculation using the  $\mathbf{k} \cdot \mathbf{p}$  method. An area in the Sn content and strain parameter space is found where a very high IVBA exists, to be avoided in good designs. Furthermore, the optimal parameters for a particular photon emission energy are found after considering the IVBA and free carrier absorption (FCA). Finally, a tensile-strained QW structure is considered and compared with a compressively strained structure. Inter-band gain and IVBA are calculated using the momentum matrix elements (MMEs) from the  $\mathbf{k} \cdot \mathbf{p}$  Hamiltonian, while FCA is calculated using an empirical bulk model suggested in Ref. 24. This should be acceptable for calculations in QWs as well, because there are no “resonant effects” for FCA in the wavelength range where the laser would be operating.

To simplify the calculation, except in Sec. III F, the Si content in the barrier layer is fixed to 10%, which is a realistic value that can be obtained by CVD growth. Another reason to choose this value is that it enables good carrier confinement even for a large Sn content (e.g., 16%) in the well.<sup>7</sup> To reduce the parameter space when searching for optimum structures, the Sn content in the barrier layer is set to be the same as that in the well layer. These choices of Si and Sn contents give a reasonable carrier confinement. Tensile strain in realistic structures can be obtained in three ways: (1) by growing the structure on an (Si)GeSn buffer layer with a larger Sn content than in the active (well) layer;<sup>25</sup> (2) by producing stress in the active layer by an SiN<sub>x</sub> stressor;<sup>22,26–28</sup> and (3) by directly applying stress, in a bridge-like structure, as presented in

Ref. 29. For the convenience of theoretical considerations, we assume that the biaxial strain in the well layer can have any value within reasonable boundaries (0%–1.7%), and then the strain in other layers was calculated accordingly, to match the stressed lattice constant in the well layer.

## II. THEORY AND METHODS

The electronic band structure around the  $\Gamma$ -point (QW states of  $\Gamma$ -electrons and of holes) and the gain/absorption coming from interband or inter-valence band transitions are here calculated by the eight-band  $\mathbf{k} \cdot \mathbf{p}$  method. The L-valley states, which are also very important for QW laser modeling, are calculated separately, by the effective mass approximation. The accuracy/reliability of material parameters needed for these calculations (particularly for alloys) has considerably improved in recent years. Certainly, the methodology and understanding of the GeSn band structure is steadily progressing over years of research. To give a few examples, when Sn content is large (~25%), the measured bandgap shows a large difference from the predictions based on the random alloy model,<sup>30,31</sup> indicating the importance of short-range order to get a better fit the experiment.<sup>32</sup> Song *et al.*<sup>33</sup> have used the 30-band  $\mathbf{k} \cdot \mathbf{p}$  method to calculate the band structure of Ge<sub>1-x</sub>Sn<sub>x</sub> in the whole Brillouin zone. Compared with the eight-band  $\mathbf{k} \cdot \mathbf{p}$  method used in this work, the higher order methods, or more precisely calculated material parameters, may generally give a better description of real structures. However, the Sn content in GeSn/SiGeSn alloys used here is limited to <15%, and the band structure near the center of the Brillouin zone is sufficient to calculate the gain spectrum; therefore, we believe that the eight-band  $\mathbf{k} \cdot \mathbf{p}$  method, together with the effective mass approximation for the L-valley, is accurate enough for the purpose of this work. Furthermore, using the finite difference method (FDM) to calculate the QW band structure is far more time-consuming than the band structure calculation for bulk material and would become much more so with the 30-band  $\mathbf{k} \cdot \mathbf{p}$  method; therefore, the eight-band  $\mathbf{k} \cdot \mathbf{p}$  should be a good realistic choice for calculations involved in structure optimization studies.

### A. Hamiltonian

We combine the  $\mathbf{k} \cdot \mathbf{p}$  method with the FDM method to calculate the band structure near the  $\Gamma$  point. The  $\mathbf{k} \cdot \mathbf{p}$  model in this work follows the theory of Kane<sup>34</sup> and Bir and Pikus<sup>35</sup> and uses the eight-band  $\mathbf{k} \cdot \mathbf{p}$  Hamiltonian derived by Bahder.<sup>36</sup>

The unstrained part is derived by substituting the Bloch function into the Schrödinger equation

$$\left[ \frac{p^2}{2m_0} + V_0 + \frac{\hbar^2 \mathbf{k}^2}{2m_0} + \frac{\hbar}{m_0} \mathbf{k} \cdot \mathbf{p} + \frac{\hbar}{4m_0^2 c^2} \nabla V_0 \times \mathbf{p} \cdot \boldsymbol{\sigma} + \frac{\hbar}{4m_0^2 c^2} \nabla V_0 \times \hbar \mathbf{k} \cdot \boldsymbol{\sigma} \right] u_{nk}(\mathbf{r}) = E_n(\mathbf{k}) u_{nk}(\mathbf{r}), \quad (1)$$

where the last term ( $\hbar \mathbf{k} \cdot \boldsymbol{\sigma}$ ) on the left is ignored in this work because the crystal momentum  $\hbar \mathbf{k}$  is much smaller than the

momentum  $\mathbf{p}$ . The inversion symmetry parameter is zero for the diamond crystal structure. We can therefore remove these zero

terms in the  $\mathbf{k} \cdot \mathbf{p}$  interaction Hamiltonian derived in Ref. 36. With the basis set

$$\begin{aligned}
 u_1 &= |S \downarrow\rangle, \\
 u_2 &= |S \uparrow\rangle, \\
 u_3 &= -\frac{i}{\sqrt{6}}(|X \downarrow\rangle + i|Y \downarrow\rangle) + i\sqrt{\frac{2}{3}}|Z \uparrow\rangle, \\
 u_4 &= \frac{i}{\sqrt{2}}(|X \uparrow\rangle + i|Y \uparrow\rangle), \\
 u_5 &= -\frac{i}{\sqrt{2}}(|X \downarrow\rangle + i|Y \downarrow\rangle), \\
 u_6 &= \frac{i}{\sqrt{6}}(|X \uparrow\rangle - i|Y \uparrow\rangle) + i\sqrt{\frac{2}{3}}|Z \downarrow\rangle, \\
 u_7 &= -\frac{i}{\sqrt{3}}(|X \uparrow\rangle - i|Y \uparrow\rangle) + \frac{i}{\sqrt{3}}|Z \downarrow\rangle, \\
 u_8 &= -\frac{i}{\sqrt{3}}(|X \downarrow\rangle + i|Y \downarrow\rangle) - \frac{i}{\sqrt{3}}|Z \uparrow\rangle,
 \end{aligned} \tag{2}$$

the matrix form of the unstrained part of the Hamiltonian is

$$\mathbf{H}(\mathbf{k}) = \begin{bmatrix} A & 0 & V^\dagger & 0 & \sqrt{3}V & -\sqrt{2}U & -U & \sqrt{2}V^\dagger \\ A & -\sqrt{2}U & -\sqrt{3}V^\dagger & 0 & -V & \sqrt{2}V & U & \\ & -P+Q & -W^\dagger & R & 0 & \sqrt{\frac{3}{2}}W & -\sqrt{2}Q & \\ & & -P-Q & 0 & R & -\sqrt{2}R & \sqrt{\frac{1}{2}}W & \\ & & & -P-Q & W^\dagger & \sqrt{\frac{1}{2}}W^\dagger & \sqrt{2}R^\dagger & \\ H.C & & & & -P+Q & \sqrt{2}Q & \sqrt{\frac{3}{2}}W^\dagger & \\ & & & & & Z & 0 & \\ & & & & & & & Z \end{bmatrix}, \tag{3}$$

where the superscript “†” denotes the Hermitian conjugate. The lower triangle of the Hamiltonian is the Hermitian conjugate (HC) of the upper part. The elements of this matrix are given by

$$\begin{aligned}
 A &= E_c + A_{cc} \frac{\hbar^2}{2m_0} (k_x^2 + k_y^2 + k_z^2), & U &= \frac{1}{\sqrt{3}} P_0 k_z, \\
 V &= \frac{1}{\sqrt{3}} P_0 (k_x - ik_y), & P &= -E_v + \gamma_1 \frac{\hbar^2}{2m_0} (k_x^2 + k_y^2 + k_z^2), \\
 Q &= \gamma_2 \frac{\hbar^2}{2m_0} (k_x^2 + k_y^2 - 2k_z^2), & R &= -\sqrt{3} \frac{\hbar^2}{2m_0} (\gamma_2 (k_x^2 - k_y^2) - 2i\gamma_3 k_x k_y), \\
 W &= \sqrt{3} \gamma_3 \frac{\hbar^2}{m_0} k_z (k_x - ik_y), & Z &= E_v - \Delta - \gamma_1 \frac{\hbar^2}{2m_0} (k_x^2 + k_y^2 + k_z^2),
 \end{aligned} \tag{4}$$

in which the momentum matrix element  $P_0$  is related to its energy form (Kane parameter) as

$$\begin{aligned}
 E_P &= \frac{2m_0}{\hbar^2} P_0^2 = \frac{2}{m_0} |\langle X | \mathbf{p}_x | S \rangle|^2 = \frac{2}{m_0} \left| \langle Y | \mathbf{p}_y | S \rangle \right|^2 \\
 &= \frac{2}{m_0} |\langle Z | \mathbf{p}_z | S \rangle|^2.
 \end{aligned} \tag{5}$$

The eight-band Luttinger parameters are related to six-band Luttinger parameters as

$$\begin{aligned}
 \gamma_1 &= \gamma_1^{(6)} - \frac{E_P}{3E_g^\Gamma + \Delta}, \\
 \gamma_{2,3} &= \gamma_{2,3}^{(6)} - \frac{E_P}{2(3E_g^\Gamma + \Delta)}.
 \end{aligned} \tag{6}$$

It is important to note that using the conventional value of  $E_P$  in the Hamiltonian gives spurious solutions. This is because of the

well-known unphysical bowing in the E-k dependence. To solve this problem,  $E_P$  is modified, according to  $E_g$ ,  $\Delta$  and electron effective mass  $m_e^*$ , through the coefficient  $A_{cc}$  (in some papers,  $A_{cc}$  may appear as “1/corrected effective mass,” and they have the same physical meaning),

$$A_{cc} = \frac{m_0}{m_e^*} - E_P \frac{E_g^\Gamma + \frac{2}{3}\Delta_{SO}}{E_g^\Gamma (E_g^\Gamma + \Delta_{SO})}. \tag{7}$$

As suggested in Ref. 37,  $A_{cc}$  is set to 1, implying that the remote bands are completely neglected, and  $E_P$  can then be calculated from Eq. (7). This new value will be different from the standard data. The value of  $E_P$  used in Ref. 7 for Ge is 26.3 eV, and the rescaled value is 24.36 eV. This is acceptable because the change is just 7.4% for the major component (Ge) in the structure, and the band structure is not very sensitive to  $E_P$ , so it is worthwhile to sacrifice some accuracy in order to eliminate spurious solutions. These solutions would not only introduce an unphysical,

non-existing band in the full band structure, but would also influence the normal wave functions in the conduction band and make them inappropriate for use in the inter-band gain calculations. For the whole procedure to be consistent, the elements  $U$  and  $V$  in Eq. (4) and eight-band Luttinger parameters in Eq. (6) also need to be recalculated using the rescaled  $E_p$ .

Regarding the strain, the orbital part of strain Hamiltonian is

$$D(\mathbf{k}) = \begin{bmatrix} a_c \varepsilon & 0 & -v^\dagger & 0 & -\sqrt{3}v & \sqrt{2}u & u & -\sqrt{2}v^\dagger \\ a_c \varepsilon & \sqrt{2}u & \sqrt{3}v^\dagger & 0 & v & -\sqrt{2}v & -u & \\ & -p+q & -w^\dagger & r & 0 & \sqrt{\frac{3}{2}}w & -\sqrt{2}q & \\ & & -p-q & 0 & r & -\sqrt{2}r & \sqrt{\frac{1}{2}}w & \\ & & & -p-q & w^\dagger & \sqrt{\frac{1}{2}}w^\dagger & \sqrt{2}r^\dagger & \\ HC & & & & -p+q & \sqrt{2}q & \sqrt{\frac{3}{2}}w^\dagger & \\ & & & & & a_v \varepsilon & 0 & \\ & & & & & & a_v \varepsilon & \end{bmatrix}, \quad (8)$$

where

$$\begin{aligned} \varepsilon &= \varepsilon_{xx} + \varepsilon_{yy} + \varepsilon_{zz}, \quad p = -a_v \varepsilon, \\ v &= \frac{1}{\sqrt{6}} P_0 \sum_j (\varepsilon_{xj} - i\varepsilon_{yj}) k_j, \quad u = \frac{1}{\sqrt{3}} P_0 \sum_j \varepsilon_{zj} k_j, \\ q &= b \left( \varepsilon_{zz} - \frac{1}{2} (\varepsilon_{xx} + \varepsilon_{yy}) \right), \quad r = \frac{\sqrt{3}}{2} b (\varepsilon_{xx} - \varepsilon_{yy}) - id\varepsilon_{xy}, \\ w &= -d (\varepsilon_{xz} - i\varepsilon_{yz}), \end{aligned} \quad (9)$$

where  $\varepsilon_{ij}$  are the strain tensor components ( $i, j = x, y$  or  $z$ ),  $a_c$  and  $a_v$  are the conduction-band and valence band deformation potentials at the  $\Gamma$  valley, and  $b$  and  $d$  are the shear deformation potentials at the  $\Gamma$  valley.

The spin-orbit part that couples the valence band to uniaxial and shear strain through the split-off energy ( $\Delta_{so}$ ) is

$$D_{so} = \frac{\Delta}{3} \begin{bmatrix} 0 & 0 \\ 0 & N_{6 \times 6} \end{bmatrix}, \quad (10)$$

where

$$N_{6 \times 6} = \begin{bmatrix} -\frac{\varepsilon}{3} - \varepsilon_{zz} & -\frac{2}{\sqrt{3}} (\varepsilon_{xz} + i\varepsilon_{yz}) & \sqrt{\frac{1}{3}} (2i\varepsilon_{xy} + \varepsilon_{yy} - \varepsilon_{xx}) & 0 & -\sqrt{\frac{1}{2}} (\varepsilon_{xz} - i\varepsilon_{yz}) & -\frac{1}{3\sqrt{2}} (3\varepsilon_{zz} - \varepsilon) \\ & \varepsilon_{zz} - \varepsilon & 0 & \sqrt{\frac{1}{3}} (2i\varepsilon_{xy} + \varepsilon_{yy} - \varepsilon_{xx}) & \frac{1}{\sqrt{6}} (2i\varepsilon_{xy} + \varepsilon_{yy} - \varepsilon_{xx}) & -\frac{1}{\sqrt{6}} (\varepsilon_{xz} - i\varepsilon_{yz}) \\ & & \varepsilon_{zz} - \varepsilon & \frac{2}{\sqrt{3}} (\varepsilon_{xz} + i\varepsilon_{yz}) & -\frac{1}{\sqrt{6}} (\varepsilon_{xz} + i\varepsilon_{yz}) & \frac{1}{\sqrt{6}} (2i\varepsilon_{xy} - \varepsilon_{yy} + \varepsilon_{xx}) \\ & & & -\frac{\varepsilon}{3} - \varepsilon_{zz} & \frac{1}{3\sqrt{2}} (3\varepsilon_{zz} - \varepsilon) & -\sqrt{\frac{1}{2}} (\varepsilon_{xz} + i\varepsilon_{yz}) \\ & & HC & & \frac{4}{3} \varepsilon & 0 \\ & & & & & \frac{4}{3} \varepsilon \end{bmatrix}. \quad (11)$$

Under strain, the total Hamiltonian matrix is obtained as the sum of Eqs. (3), (8), and (11). For biaxial strain, when a layer is grown on a lattice-mismatched substrate,  $\varepsilon_{xy} = \varepsilon_{xz} = \varepsilon_{yz} = 0$ ,  $\varepsilon_{xx} = \varepsilon_{yy} = (a_0 - a)/a$ ,  $\varepsilon_{zz} = -2C_{12}\varepsilon_{xx}/C_{11}$ ,  $a_0$  and  $a$  are the relaxed cubic lattice constants of the substrate and the layer grown on it.

To apply the FDM to a QW system, considering the structure grown in the [001] direction, the wave vector  $\mathbf{k}_z$  becomes an operator  $-i\partial/\partial z$ . Using the finite difference schemes, with  $n$  mesh points in the  $z$  direction, we get an  $8n \times 8n$  sparse matrix. The eigenvalues and eigenvectors of this matrix were calculated using the LAPACK library,<sup>40</sup>

$$g(z) \frac{\partial}{\partial z} F(z) = \frac{g_i(F_{i+1} - F_{i-1})}{2\Delta z}, \quad g(z) \frac{\partial^2}{\partial z^2} F(z) = \frac{\partial}{\partial z} g(z) \frac{\partial}{\partial z} F(z) = \frac{(g_{i+1} + g_i)F_{i+1} - (g_{i+1} + 2g_i + g_{i-1})F_i + (g_i + g_{i-1})F_{i-1}}{2(\Delta z)^2}. \quad (12)$$

The first order terms with  $P\mathbf{k}_z$  preserve the order as in the original matrix. The conventional “Hermitian symmetrizing” [(i.e.,  $P\mathbf{k}_z = (P\mathbf{k}_z + \mathbf{k}_z P)/2$ ] is inappropriate, as has been previously discussed by Luttinger and Foreman.<sup>38,39</sup>

Equation (12) is also used to solve the effective-mass Schrödinger equation for the L-valley

$$-\frac{\hbar^2}{2} \frac{\partial}{\partial z} \frac{1}{m_q^L(z)} \frac{\partial}{\partial z} \psi^L(z) + V^L(z) \psi^L(z) = E^L \psi^L(z), \quad (13)$$

in which  $m_q^L$  is the quantization effective mass. The potential profile under strain was calculated as

$$V_\varepsilon^L = E_v + E_g^L + a_L \varepsilon, \quad (14)$$

in which  $\varepsilon = \varepsilon_{xx} + \varepsilon_{yy} + \varepsilon_{zz}$ ,  $E_v$  is the valence band offset,  $E_g^L$  is the bandgap toward the L-valley, and  $a_L$  denotes the L-valley deformation potential. The data for the deformation potentials are given in Sec. II C.

## B. Gain calculation

Gain and absorption were calculated for a given carrier density. The injected carrier densities for electrons and holes are equal, while N-doping or P-doping provides additional carrier density of electrons or holes. The 2D carrier densities in quantized states of the conduction band and valence band are

$$N_{2D} = \frac{1}{4\pi^2} \sum_i^{n_r} \iint d\mathbf{k}_\parallel \left[ 1 + \exp\left(\frac{E_i^c(\mathbf{k}_\parallel) - E_{fc}}{k_B T}\right) \right] + 4 \frac{m_d^L k_B T}{\pi \hbar^2} \sum_i^{n_l} \ln \left[ 1 + \exp\left(\frac{E_{fc} - E_i^v}{k_B T}\right) \right], \quad (15)$$

$$P_{2D} = \frac{1}{4\pi^2} \sum_i^{n_v} \iint d\mathbf{k}_\parallel \left[ 1 + \exp\left(\frac{E_{fv} - E_i^v(\mathbf{k}_\parallel)}{k_B T}\right) \right]. \quad (16)$$

The first term in Eqs. (15) and (16) describes the carriers near the center of the Brillouin zone. The  $E$ - $k$  relations for these states in the QW were calculated by the  $\mathbf{k} \cdot \mathbf{p}$  method. The second term in Eq. (15) is the 2D carrier density in L-valley states. This term is multiplied by four because there are eight identical half-valleys in the [111] directions in the first Brillouin zone. Since the L-valley states were calculated by EMM, we used the parabolic approximation for  $E$ - $k$  dependence.  $m_d^L$  is the 2D density of states effective mass. Density of states effective mass and quantization effective mass used in the EMM were calculated from the longitudinal and transverse effective masses as  $m_d^L = \sqrt{(2m_l m_t + m_l^2)}/3$ ,  $m_q^L = 3m_l m_t / (2m_l + m_t)$ .<sup>41</sup> The  $\Delta$ -valleys are not included in this calculation because their energy is much higher than that of  $\Gamma$  and L valleys in the GeSn alloy. Moreover, the GeSn layer is not a potential well for  $\Delta$ -valleys in SiGeSn/GeSn/SiGeSn QWs.

The inter-band absorption (IBA) and inter-valence band absorption (IVBA) were calculated from

$$\alpha_\sigma(\hbar\omega) = \frac{\pi q^2}{n_r c \varepsilon_0 m_0^2 \omega L_w} \sum_{s,t} \iint d\mathbf{k}_\parallel \frac{2}{(2\pi)^2} |\langle \Psi_s | \widehat{\mathbf{p}}_\sigma | \Psi_t \rangle|^2 \times \delta(E_{s,t}(\mathbf{k}_\parallel), \hbar\omega) (f_t(\mathbf{k}_\parallel) - f_s(\mathbf{k}_\parallel)), \quad (17)$$

in which  $q$  is the electron charge,  $n_r$  is the refractive index,  $c$  is the speed of light,  $\varepsilon_0$  is the vacuum permittivity,  $m_0$  is the free electron mass, and  $L_w$  is the QW width.  $s$  and  $t$  are the subband indices. For IBA,  $s$  represents the conduction band and  $t$  the LH/HH bands. For inter-valence band absorption,  $s$  denotes LH/HH bands and  $t$  the split-off band.  $\sigma$  denotes the polarization, for TM  $\sigma = z$  and for TE  $\sigma = x, y$ . The momentum matrix element (MME) was calculated as

$$\langle \Psi_s | \widehat{\mathbf{p}}_\sigma | \Psi_t \rangle = \sum_i \langle F_{s,i}(z, \mathbf{k}_\parallel) | \widehat{\mathbf{p}}_\sigma | F_{t,i}(z, \mathbf{k}_\parallel) \rangle + \sum_{ij} \langle F_{s,i}(z, \mathbf{k}_\parallel) | F_{t,i}(z, \mathbf{k}_\parallel) \rangle \langle u_i | \widehat{\mathbf{p}}_\sigma | u_j \rangle, \quad (18)$$

where  $u_i$  and  $u_j$  are the basis states from Eq. (2), and  $F(z, \mathbf{k}_\parallel)$  is the envelope function of the corresponding basis state. This expression can be further approximated by ignoring the first term, because  $\hbar k$  is much smaller than  $(m_0/\hbar)P$ . Non-zero terms in MME come from s orbital on one and p orbital on the other side. The difference in Fermi-Dirac distributions  $f_t - f_s$  is the Fermi-Dirac inversion factor, and if this value is negative then a negative absorption  $\alpha_\sigma(\hbar\omega) < 0$ , i.e., a positive gain will be observed. The Fermi-Dirac distribution is

$$f_{s,t}(\mathbf{k}_\parallel) = \left[ 1 + \exp\left(\frac{E_{s,t}(\mathbf{k}_\parallel) - E_f^{s,t}}{k_B T}\right) \right]^{-1}. \quad (19)$$

The quasi-Fermi levels in Eq. (19) were calculated from Eqs. (15) and (16). For IBA,  $E_f^s = E_{fc}$ ,  $E_f^t = E_{fv}$ . For IVBA, both of them are the valence band quasi-Fermi level.

Integrals with the delta function in the expression for absorption were calculated by a quadratic simplex method, to reduce the computation time.<sup>42</sup> Lorentzian line shape function is then used to smooth the numerical instability. Full width half maximum (FWHM) of the Lorentzian is taken as 5 meV for IBA and 20 meV for IVBA. FWHM for IVBA is taken larger because the SO states are much deeper in the valence band, they will “entangle” (mix) with free LH and HH states. In actual FDM based calculations, these free states are not in continuum and they are formally discrete and are filtered out in order to reduce the artificial effects in results as much as possible. An SO subband thus calculated will be discontinuous, as the in-plane wave vector varies, because of these free states, which will cause discontinuities in the absorption spectrum. However, we found that after convolution with a Lorentzian function with a reasonably large FWHM, the results for IVBA will not be very sensitive to the numerical settings.

Free carrier absorption is an important loss mechanism for high injected carrier density and doping. In this work, the 2D carrier densities for both electrons and holes are around  $4 \times 10^{12} \text{ cm}^{-2}$ . QW width is around 15 nm, which makes the equivalent 3D carrier density of the order of  $10^{18} \text{ cm}^{-3}$ . In Ref. 43, an empirical formula is given to estimate FCA for pure Ge, at 300 K, depending on the carrier densities

$$\alpha_{FCA}(\lambda) = -1.7 \times 10^{-25} \times N_v \lambda^{2.25} + -3.2 \times 10^{-25} \times P_v \lambda^{2.43}, \quad (20)$$

in which  $\lambda$  is in units of nm,  $N$  and  $P$  are in units of  $\text{cm}^{-3}$ , and  $\alpha$  is in units of  $\text{cm}^{-1}$ . We have used this expression to approximate the FCA in QW structures considered here, and the 3D (volume) carrier densities are taken as  $N_v = N_{2D}/L_w$  and  $P_v = P_{2D}/L_w$ .

### C. Parameters

SiGeSn is a ternary alloy. The parameters of SiGeSn can be roughly estimated by taking the weighted average of the parameters of pure elements. However, in many cases, this is not very accurate, and to match the realistic data obtained from experiments or calculated by atomistic methods, the bowing parameters are also included. Then, a parameter can be calculated as

$$G_{\text{SiGeSn}} = \eta_{\text{Si}} G_{\text{Si}} + \eta_{\text{Ge}} G_{\text{Ge}} + \eta_{\text{Sn}} G_{\text{Sn}} - \eta_{\text{Si}} \eta_{\text{Ge}} B_{\text{SiGe}} - \eta_{\text{Si}} \eta_{\text{Sn}} B_{\text{SiSn}} - \eta_{\text{Ge}} \eta_{\text{Sn}} B_{\text{GeSn}}, \quad (21)$$

where  $B$  is the bowing parameter for two components and  $\eta_{\text{Si}}$ ,  $\eta_{\text{Ge}}$ , and  $\eta_{\text{Sn}}$  denote the mole fraction. The research study on bowing was mostly focused on GeSn, while the bowing for SiGe and SiSn was studied less frequently. Parameters of pure elements are given in Table I.

In this work, parameters using linear interpolation are  $a_c$ ,  $a_v$ ,  $b$ ,  $d$ ,  $a_L$ ,  $C_{11}$ ,  $C_{12}$ ,  $C_{44}$ , and  $n_r$ . The bowing parameters are found for the lattice constant, see Table II.

For other parameters, only the bowing for GeSn could be found, in some cases this is in the form of interpolation parameters. For the ternary alloy, we used interpolation to calculate the parameters for GeSn, and then linear interpolation according to the silicon content,

$$G_{\text{SiGeSn}} = \left[ \xi_{\text{GeSn}} + \beta_{\text{GeSn}} \frac{\eta_{\text{Ge}}}{1 - \eta_{\text{Si}}} + \chi_{\text{GeSn}} \left( \frac{\eta_{\text{Ge}}}{1 - \eta_{\text{Si}}} \right)^2 \right] (1 - \eta_{\text{Si}}) + G_{\text{Si}} \eta_{\text{Si}}, \quad (22)$$

in which  $\xi$ ,  $\beta$ , and  $\chi$  are the zeroth, first, and second order interpolation parameters. Their values are given in Table III. The six-band Luttinger parameters for SiGe are not described by bowing parameters,<sup>49</sup> so Eq. (22) cannot be directly used. In this work, we found that ignoring the bowing of SiGe caused unnatural splitting of energy levels with different spins, the reasons for this are unclear, but including the bowing of SiGe parameters gives a more accurate

TABLE I. Parameters of pure Si, Ge, and Sn.

Parameter	Symbol	Si	Ge	Sn
Lattice constant	$a_{\text{lat}}(\text{\AA})$	5.4307 <sup>a</sup>	5.6579 <sup>a</sup>	6.489 <sup>a</sup>
Bandgap ( $\Gamma$ )	$E_g^\Gamma(\text{eV})$	4.185 <sup>a</sup>	0.89 <sup>b</sup>	-0.38 <sup>b</sup>
Bandgap (L)	$E_g^L(\text{eV})$	2.716 <sup>a</sup>	0.74 <sup>b</sup>	0.1 <sup>b</sup>
Split-off energy	$\Delta_{\text{so}}(\text{eV})$	0.044 <sup>a</sup>	0.26 <sup>b</sup>	0.6 <sup>b</sup>
Six-band Luttinger	$\gamma_1$	4.285 <sup>a</sup>	13.38 <sup>a</sup>	-12 <sup>a</sup>
Six-band Luttinger	$\gamma_2$	0.339 <sup>a</sup>	4.24 <sup>a</sup>	-8.45 <sup>a</sup>
Six-band Luttinger	$\gamma_3$	1.446 <sup>a</sup>	5.69 <sup>a</sup>	-6.84 <sup>a</sup>
Momentum energy	$E_p(\text{eV})$	21.6 <sup>a</sup>	26.3 <sup>a</sup>	23.8 <sup>a</sup>
Valence band offset	$E_v(\text{eV})$	-1.86 <sup>c</sup>	-0.91 <sup>b</sup>	0 <sup>c</sup>
Pikus-Bir DP	$a_c(\text{eV})$	-10.06 <sup>a</sup>	-8.24 <sup>a,d</sup>	-6 <sup>a</sup>
Pikus-Bir DP	$a_v(\text{eV})$	2.46 <sup>a</sup>	1.24 <sup>a</sup>	1.58 <sup>a</sup>
Pikus-Bir DP	$b(\text{eV})$	-2.1 <sup>a</sup>	-2.9 <sup>a</sup>	-2.7 <sup>a</sup>
Pikus-Bir DP	$d(\text{eV})$	-5.3 <sup>d</sup>	-4.8 <sup>d</sup>	-4.1 <sup>d</sup>
L-valley DP	$a_L(\text{eV})$	-0.66 <sup>a</sup>	-1.54 <sup>a</sup>	-2.14 <sup>a</sup>
Stiffness constant	$C_{11}(\text{GPa})$	165.77 <sup>a</sup>	128.53 <sup>a</sup>	69 <sup>a,d</sup>
Stiffness constant	$C_{12}(\text{GPa})$	63.93 <sup>a</sup>	48.26 <sup>a</sup>	29.3 <sup>a,d</sup>
Stiffness constant	$C_{44}(\text{GPa})$	79.51 <sup>d</sup>	66.7 <sup>d</sup>	36.2 <sup>d</sup>
Effective mass ( $\Gamma$ )	$m_e^\Gamma(m_0)$	0.188 <sup>d</sup>	0.038 <sup>d</sup>	-0.058 <sup>d</sup>
Longitudinal effective mass (L)	$m_l^L(m_0)$	1.418 <sup>d</sup>	1.61 <sup>d</sup>	1.478 <sup>d</sup>
Transverse effective mass (L)	$m_t^L(m_0)$	0.13 <sup>d</sup>	0.081 <sup>d</sup>	0.075 <sup>d</sup>
Refractive index ( $4.1 \mu\text{m}$ )	$n_r$	3.4 <sup>e</sup>	4 <sup>e</sup>	6.18 <sup>f</sup>

<sup>a</sup>Reference 7.

<sup>b</sup>Reference 1.

<sup>c</sup>Reference 44.

<sup>d</sup>Reference 45.

<sup>e</sup>Reference 46.

<sup>f</sup>Reference 47.

<sup>g</sup>Reference 6.

band structure. The bowing for SiGe is included as

$$\gamma_{\text{SiGeSn}} = \left\{ \left[ \xi_{\text{GeSn}}^\gamma + \beta_{\text{GeSn}}^\gamma \frac{\eta_{\text{Ge}}}{1 - \eta_{\text{Si}}} + \chi_{\text{GeSn}}^\gamma \left( \frac{\eta_{\text{Ge}}}{1 - \eta_{\text{Si}}} \right)^2 \right] \times (1 - \eta_{\text{E}}) + \gamma_{\text{Si}} \eta_{\text{Si}} \right\} \left\{ \frac{\gamma_{\text{Si}_{[\text{Sn}/(1-\eta_{\text{Sn})}] \text{Ge}}^{\text{bow}}}}{\gamma_{\text{Si}_{[\text{Sn}/(1-\eta_{\text{Sn})}] \text{Ge}}^{\text{linear}}}} \right\}, \quad (23)$$

TABLE II. Bowing parameter of lattice constant.<sup>7</sup>

$B_{\text{SiGe}}$	$B_{\text{GeSn}}$	$B_{\text{SiSn}}$
0.026	-0.041	0

TABLE III. Interpolation parameters for GeSn.

Interpolation	$\xi$	$\beta$	$\chi$
$E_g^\Gamma$ (eV)	0.89 <sup>a</sup>	-4.29 <sup>a</sup>	3.02 <sup>a</sup>
$E_g^L$ (eV)	0.74 <sup>a</sup>	-1.87 <sup>a</sup>	1.23 <sup>a</sup>
$\Delta_{so}$ (eV)	0.26 <sup>a</sup>	0.24 <sup>a</sup>	0.1 <sup>a</sup>
$\gamma_1$	11.11 <sup>b</sup>	28.53 <sup>b</sup>	105.2 <sup>b</sup>
$\gamma_2$	3.252 <sup>b</sup>	13.95 <sup>b</sup>	52.75 <sup>b</sup>
$\gamma_3$	4.689 <sup>b</sup>	14.37 <sup>b</sup>	52.57 <sup>b</sup>
$E_p$ (eV)	25.61 <sup>b</sup>	-2.319 <sup>b</sup>	0.2463 <sup>b</sup>
$E_v$ (eV)	-0.91 <sup>a</sup>	0.32 <sup>a</sup>	0.59 <sup>a</sup>
$m_e^\Gamma$ ( $m_0$ )	0.042 <sup>b</sup>	-0.1436 <sup>b</sup>	0.1026 <sup>b</sup>
$m_l^\Gamma$ ( $m_0$ )	1.5929 <sup>b</sup>	-0.0642 <sup>b</sup>	-0.1087 <sup>b</sup>
$m_l^L$ ( $m_0$ )	0.0922 <sup>b</sup>	-0.0561 <sup>b</sup>	0.0146 <sup>b</sup>

<sup>a</sup>Calculated from bowing in Ref. 1.

<sup>b</sup>Reference 48.

where  $\gamma_{SiGe}^{bow}$  is a Luttinger parameter after applying bowing for SiGe, with Si content of  $\eta_{Si}/(1 - \eta_{Sn})$ , and  $\gamma_{SiGe}^{lin}$  is the corresponding value from linear interpolation.  $\gamma_{SiGe}^{bow}$  are estimated, as in Ref. 49, from

$$\begin{aligned} \gamma_1 &= \frac{E_p}{3E_0} + \frac{2E'_p}{3E'_0} + \bar{\gamma}_1, \\ \gamma_2 &= \frac{E_p}{6E_0} - \frac{E'_p}{6E'_0} + \bar{\gamma}_2, \\ \gamma_3 &= \frac{E_p}{6E_0} + \frac{E'_p}{6E'_0} + \bar{\gamma}_3, \end{aligned} \quad (24)$$

in which  $\bar{\gamma}_1$ ,  $\bar{\gamma}_2$ , and  $\bar{\gamma}_3$  are linear interpolation values between pure Si and Ge. Note that these are not true Luttinger parameters. They are just the values calculated from other parameters for pure Si and Ge.  $E'_p$  is Kane's momentum matrix element describing the coupling between  $\Gamma_{25}$  band and  $\Gamma_{15}$  band.  $E'_0$  is the bandgap between  $\Gamma_{25}$  band and  $\Gamma_{15}$  band. Parameters used in Eq. (24) are listed in Table IV.

The bowing parameters of SiSn in this work are set to 0 because of the lack of reliable data. For some parameters, the bowing is intrinsically zero (e.g., the lattice constant).<sup>50</sup> For other

TABLE IV. Parameters used to calculate bowing of Luttinger parameters of SiGe.

Parameters	Si	Ge
$\bar{\gamma}_1$	-0.2589 <sup>a</sup>	-0.1159 <sup>a</sup>
$\bar{\gamma}_2$	0.2357 <sup>a</sup>	0.3030 <sup>a</sup>
$\bar{\gamma}_3$	-0.1201 <sup>a</sup>	-0.1243 <sup>a</sup>
$E'_p$ (eV)	14.4 <sup>b</sup>	17.5 <sup>b</sup>
$E'_0$ (eV)	3.4 <sup>b</sup>	3.124 <sup>b</sup>

<sup>a</sup>Calculated.

<sup>b</sup>Reference 49.

parameters, some research studies do indicate the existence of bowing in these parameters (e.g.,  $\Gamma$ -bandgap<sup>51</sup> and L-bandgap).<sup>52</sup> But since the silicon content in this work is 0–0.1, and the Sn content is less than  $\sim 0.15$ , we assumed that the deviation caused by such bowing is acceptable because the most important, well layer does not have any Si content. Although such a difference in barrier could affect the carrier confinement, for the parameter space studied in this work this is not the major effect. Furthermore, the difference for SiGeSn (barrier) will also be much smaller than for binary SiSn considering the coefficient of the bowing term ( $\eta_{Si}\eta_{Sn}$ ).

Note that the valence band profile is handled by assuming  $E_v^{Sn} = 0$  as a reference point.  $E_v^{Si}$  and  $E_v^{Ge}$  are recalculated according to the valence band offset of Si/Sn and Ge/Sn from Refs. 1 and 44. The valence band offset of SiGeSn/GeSn alloys can further be obtained by using the bowing parameters in Ref. 1, and calculated by Vegard's law.

### III. RESULTS AND DISCUSSION

#### A. Electronic properties

Figure 1 shows the photon emission energy (i.e.,  $E_{c1} - E_{v1}$ ) of a 15 nm QW for different Sn content and strain values. Unlike bulk material, in which HH and LH are degenerate at the  $\Gamma$  point, in an

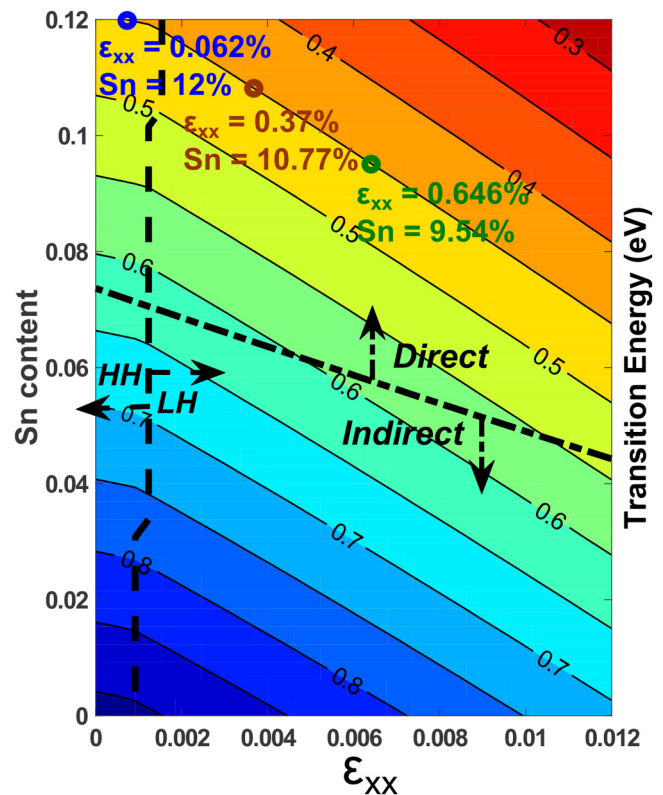


FIG. 1. Transition energies ( $\Delta E_1 = E_{c1} - E_{v1}$ ) of a 15 nm SiGeSn/GeSn QW in  $\epsilon_{xx}$ -Sn content parameter space.

unstrained QW the first quantized HH state is higher than the LH state. In such a structure, a good TE gain may be observed. When tensile strain is introduced, LH will become higher than the HH band at the  $\Gamma$  point, and for a sufficiently large strain the quantization effects may not keep HH as the first state in the valence band, LH will become the first state instead. For a large tensile strain (e.g.,  $\epsilon_{xx} = 0.6\%$ ), the first LH state will be far away from other states, and the gain will be dominant for TM polarization. The indirect-direct transition boundary is also shown in Fig. 1. It will also be different (“higher” in Fig. 1) from that of bulk material because of quantization effects. In the conduction band, the quantization energy is larger for  $\Gamma$  than for L electrons, so for smaller well widths the structure becomes more indirect. Hence, a narrow well width is unfavorable for gain.

It is clear that the same transition energy can be achieved with various combinations of parameters. For example, the three marked points in Fig. 1 will all give a photon emission energy of 0.45 eV. The band structures for these cases are shown in Fig. 2. The types of the bands are classified by checking the dominant part of the envelope wave functions at the center of the Brillouin zone. The energy difference between the first state of L-valley and  $\Gamma$ -valley ( $E_{c1}^L - E_{c1}^\Gamma$ ) is 97.7 meV, when  $\epsilon_{xx}$  is 0.062% and the Sn content is 12%. For the third case,  $\epsilon_{xx} = 0.646\%$  and Sn = 9.54%, ( $E_{c1}^L - E_{c1}^\Gamma$ ) is 91.1 meV. The difference becomes smaller (“less direct material”) for larger strain and smaller Sn content. Therefore, for the same transition energy, a higher Sn content will make the band structure more direct. On the other hand, higher

strain will make LH1 further away from other states, and more carriers will populate the first subband, for a constant carrier density, which is also good for gain. The trade-off between strain and Sn content is analyzed in this work. The optimum combinations of strain, Sn content, and well width are given, as a guideline for promising lasing structures. Although stressors like SiN usually produce a relatively narrow range of tensile strains in the structure, one can expect that the strain can be tuned in a broader range by appropriate design. The inter-band group-IV QW lasers would then be possible for a range of wavelengths.

## B. Well width

In Fig. 3, four typical structures are used to determine the optimum range of well widths for gain at room temperature (300 K). The calculations are done for 8–21 nm well width, with a step of 1 nm. The first structure has no strain in the well layer and the Sn content is 12%. In this structure, a significant TE mode gain will be achieved for a carrier density of  $4 \times 10^{12} \text{ cm}^{-2}$ . Some TM gain will also exist, just because of the coupling of LH and HH states. For the second structure, HH1 is very close to LH1, and the polarization for which the gain is larger will change when increasing the well width gradually. The third and fourth structures have relatively large tensile strain ( $\epsilon_{xx} = 0.7\%$  and  $\epsilon_{xx} = 1\%$ ), TM will be the major polarization, and the photon emission energy will be relatively low. Here we use the dimensionless gain (the product of gain and well width) to eliminate the influence of the well width

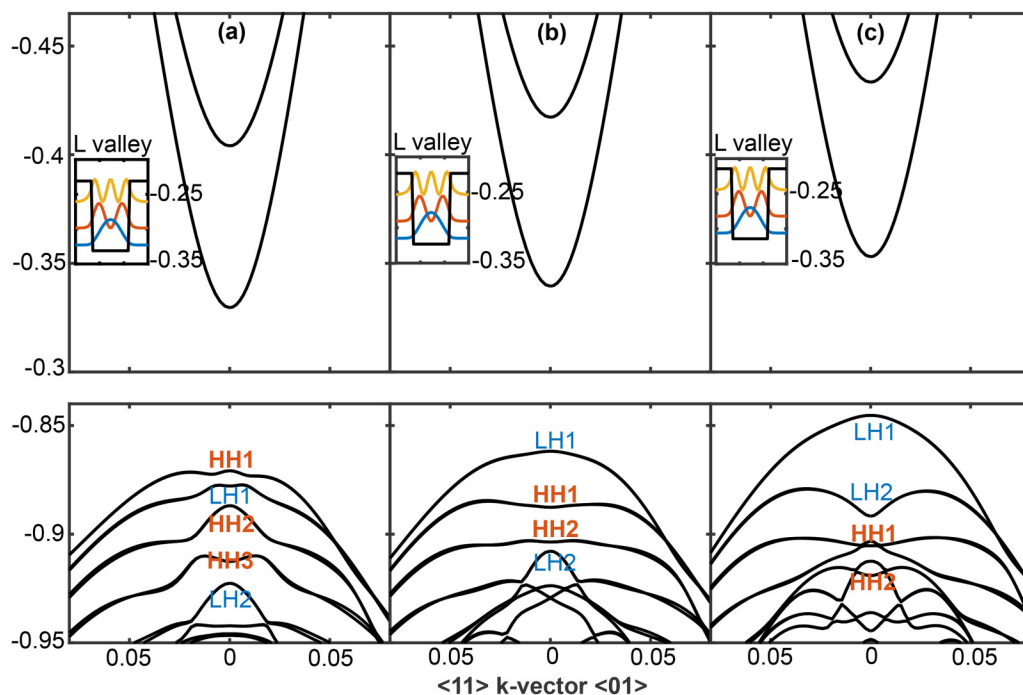


**FIG. 2.** Band structure of a 15 nm wide GeSn/SiGeSn QW with a similar photon emission energy (a)  $\epsilon_{xx} = 0.062\%$ , Sn content = 12%, (b)  $\epsilon_{xx} = 0.37\%$ , Sn = 10.77%, and (c)  $\epsilon_{xx} = 0.646\%$ , Sn = 9.54%.

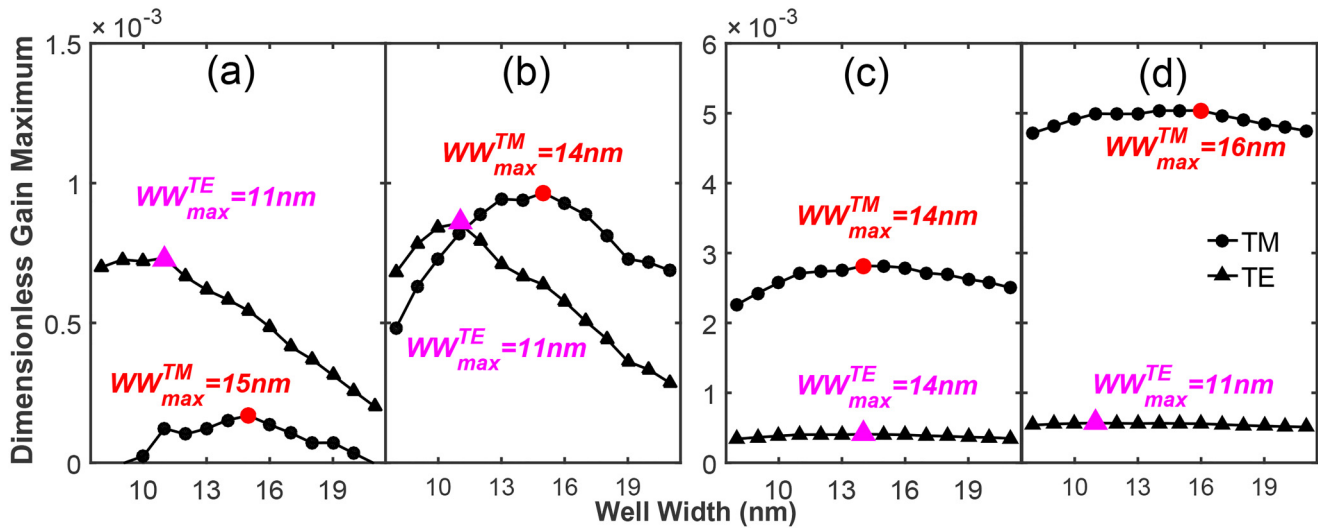


FIG. 3. The maximum gain vs well width dependence. The maximum points for TE and TM polarization are denoted by purple and red dots. (a)  $\epsilon_{xx} = 0\%$ , Sn content = 12%, (b)  $\epsilon_{xx} = 0.15\%$ , Sn content = 12%, (c)  $\epsilon_{xx} = 0.7\%$ , Sn content = 10%, and (d)  $\epsilon_{xx} = 1\%$ , Sn content = 10%.

itself on the result. In Fig. 3, in the first structure, the TE mode is dominant, and the maximum appears for 11 nm width. In the second structure, the TE gain is larger than TM when well width is smaller than 11.5 nm, and TM is larger than TE for well widths over 11.5 nm. The maximum gain appears at 11 nm for the TE mode and 14 nm for the TM mode. In the third and fourth structures, the TM mode is dominant, and maximum gain appears at 14 and 16 nm. All these lines show a trend of gain first increasing with the well width and then decreasing after the peak point. The gain is lower for narrow wells because the L-valley has a larger effective mass than the  $\Gamma$ -valley. So, the band structure is less direct for narrow QWs, and more electrons will populate the L-valley. The fraction of electrons populating the  $\Gamma$ -valley for an 8 nm QW is 18.7%, 22.0%, 21.5%, and 28.0% for the four cases, but these increase to 29.4%, 34.6%, 34.2%, and 45.0% for 21 nm QW. However, a wide well may not always give a large gain, because a larger number of quantized states become too low in energy, and well populated with carriers at 300 K. Higher states give little contribution to gain, because transitions between states with different quantum numbers are weak, and the spacing between the second quantized states of the conduction and valence bands  $\Delta E_2$  is always much higher than  $\Delta E_f$  for a carrier density of  $4 \times 10^{12} \text{ cm}^{-2}$ , as shown in Fig. 4. Gain exists for photon energies between  $\Delta E_1$  and  $\Delta E_f$ , and if HH1 and LH1 are not very near each other, changing the well width will not have a big influence on the value of  $\alpha_0$  for the main polarization. The gain is determined by  $\alpha_0(f_c - f_v)$ , and the maximum value will be proportional to  $\Delta E_1 - \Delta E_f$ .

So, if the gain is predominantly present for one polarization, the maximum gain is strongly related to the difference of  $\Delta E_1$  and  $\Delta E_f$ . We can also see that the dimensionless gain maximum decreases faster with the well width for structures with lower strain. Structures giving TE gain are more sensitive to increasing well

width, because these structures will usually have a small strain in the well layer, and in this case HH subbands are near to each other than LH, which contributes to this negative effect and makes the gain more sensitive to the well width. By testing different combinations of strain and Sn content, we find that 11–12 nm will usually give the highest TE mode gain for structures with low tensile strain

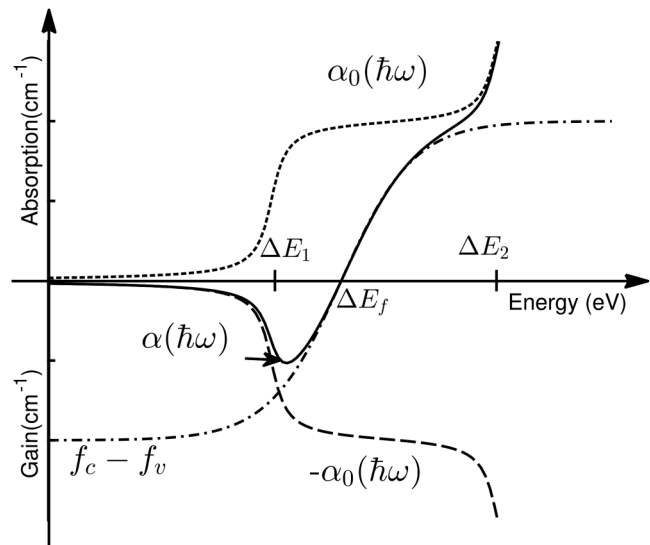


FIG. 4. The absorption spectrum  $\alpha(\hbar\omega)$ , with gain existing for photon energies between  $\Delta E_1$  and  $\Delta E_f$ .

(i.e., with HH1 higher than LH1). In addition, 13–16 nm is a good choice for high tensile strain structures to deliver the TM mode gain.

### C. Gain and absorption spectrum

Figure 5(a) shows the gain spectra at 300 K calculated by the  $\mathbf{k} \cdot \mathbf{p}$  method. The well width is taken as 14 nm and the carrier density is  $4 \times 10^{12} \text{ cm}^{-2}$  (for a 14 nm QW, the corresponding 3D carrier density is  $2.86 \times 10^{18} \text{ cm}^{-3}$ ). We have here chosen, as examples, three Sn contents (8%, 9.56%, and 11.1%) and tensile strain vary from 0.3% to 1.1%. It is clear that higher Sn contents and higher strains give higher peak gains, though at a lower photon energy. Figure 5(b) gives the losses from FCA and IVBA. The FCA is calculated from the bulk model and increases smoothly when transition energy decreases. For the parameters chosen here, the IVBA is strong between 0.35 and 0.45 eV. IVBA does not exist at low energies, below 0.26 eV, because the spin split-off band energy in Ge is 0.26 eV. Mixing with Sn, or introducing tensile strain, will only make this value larger. The absorption can also take place between LH and HH states, but the transition energy is too low to make any difference to the gain spectrum of interest. Although the

temperature and carrier density are fixed in this case, the upper energy boundary of the range where IVBA can be observed is determined by the hole density and temperature. If the hole density is large or the temperature is high, states with larger  $k_{\parallel}$  will be populated and the absorption can exist at higher photon energies.

Taking the loss mechanisms into consideration, Fig. 5(a) also gives the net gains for these structures (thick solid lines). The TE mode gain disappeared because the inter-band gain for it does not exceed the loss from IVBA and FCA. So, we are mostly interested in the TM mode here. For the TM mode, the difference between net gain and inter-band gain is found to be the largest around 0.4 eV. Because of the limited range of parameters, the largest tensile strain here is 1.1%, and when the Sn content is 8%, it cannot have gain at energy lower than 0.425 eV. Also, for the Sn content of 9.56%, the emission energy cannot be lower than 0.37 eV. Due to these aspects, it is then not simple to anticipate what combination is better just from the gain spectra. In order to find the highest TM gain for a given photon emission energy, the values of IVBA + FCA at photon emission energy are analyzed using more points in the parameter space. The combinations of parameters that offer the highest net gain for a given photon emission energy are discussed in Secs. III D and III E.

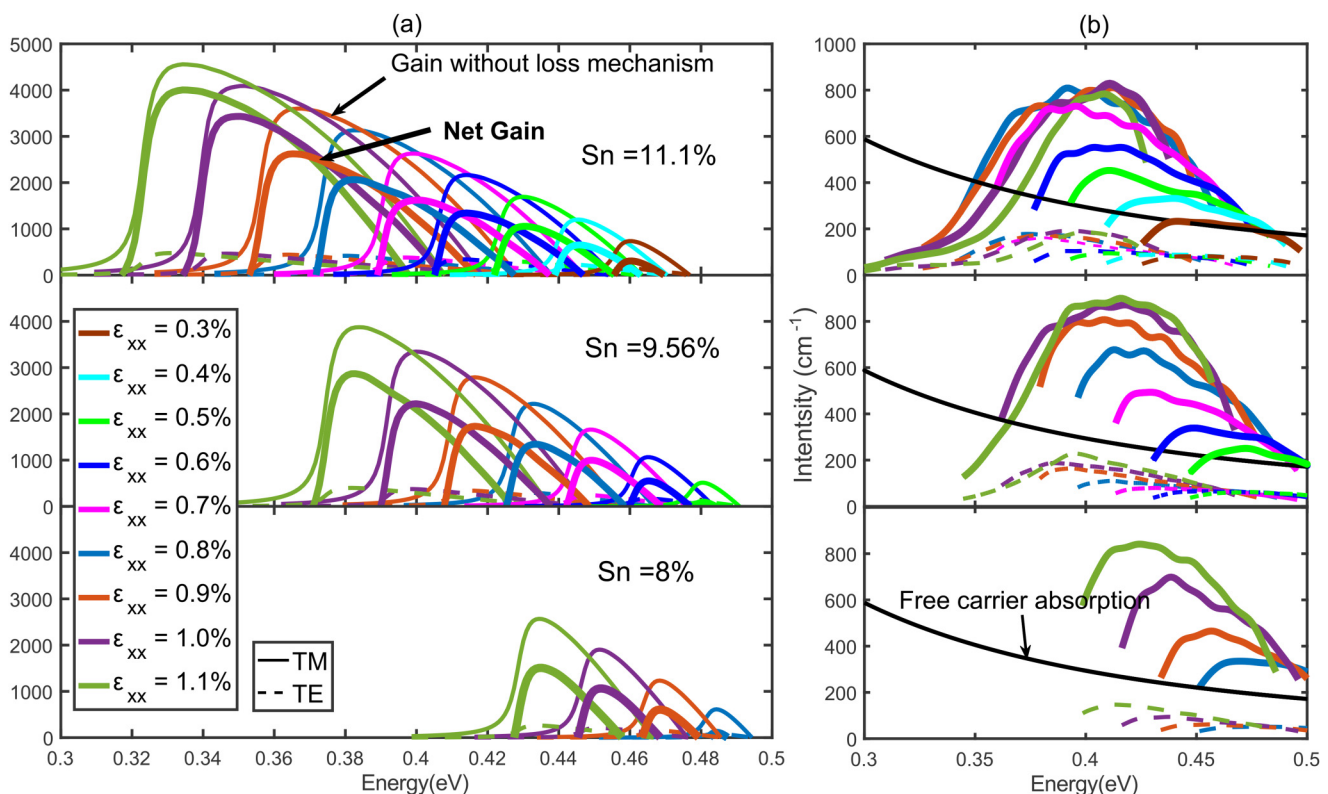


**FIG. 5.** (a) Gain spectra of 14 nm wide GeSn/SiGeSn QW with 2D carrier density of  $4 \times 10^{12} \text{ cm}^{-2}$  for Sn contents of 8%, 9.56%, and 11.1% under biaxial strain from 0.3% to 1.1% and (b) the corresponding inter-valence band absorption and free carrier absorption.

#### D. Loss mechanisms

In order to analyze the impact of IVBA and FCA on the gain, the value of absorption at photon emission energy (that a particular combination of structure parameters will give) is illustrated in Fig. 6. The well width used here is 14 nm, and the temperature is 300 K. The range of tensile strain is set to 0.3%–1.2%, and the range of Sn content is 6.056%–11.5%. We use contour lines at 80% of the maximum value of losses in this parameter space to show the region where the highest losses will appear. The position of this high-loss region is relatively insensitive to carrier density, and the combination of parameters for the highest loss can be approximated by  $\text{Sn}(\%) = -7.71\epsilon_{xx}(\%) + 17.13$ . The 80% contour lines for different well widths, with  $4 \times 10^{12} \text{ cm}^{-2}$  carrier density, are also given in Fig. 6(b). It is clear that, in the range 12–16 nm, the well width does not have a strong influence on the high-loss region. We should also note that the accuracy of the result presented here is limited by the eight-band  $\mathbf{k} \cdot \mathbf{p}$  method and by “numerical noise” from the finite difference method. As reported in Ref. 53, the IVBA from  $\mathbf{k} \cdot \mathbf{p}$  calculations for GaAs is smaller than that found experimentally, and it may be reasonable to assume the same for GeSn. Therefore, one may expect somewhat higher values in the displayed parameter space, but the range where high losses exist should remain the same.

#### E. Optimum choice of Sn content and strain

An example of a 14 nm QW, with Sn content from 6.056% to 11.5%, and strain  $\epsilon_{xx}$  from 0.3% to 1.7%, is used here to show how the optimum points are distributed in Sn- $\epsilon_{xx}$  parameter space at room temperature. Figure 7 shows the maximum net gain after including the loss mechanisms from IVBA and FCA, for different carrier densities. Optimum points are found using interpolation, and the usable areas are estimated by polynomial regression and statistic border. The “ridge” of high loss, spanning the strain/

Sn-content parameter space, which is mentioned in Sec. III D, is also shown in Fig. 7. It is obvious that for carrier densities from  $3 \times 10^{12} \text{ cm}^{-2}$  to  $5 \times 10^{12} \text{ cm}^{-2}$ , the high-loss region splits the range of usable material parameters into two areas. A few points landed in the high-loss region, and the material parameters in this range should be avoided. For the required photon energy higher than 420 meV, since the range of parameters that produce net gain is also limited by the carrier density, the recommended combinations also vary with the carrier density. We find that for the carrier density from  $4 \times 10^{12}$  to  $5 \times 10^{12} \text{ cm}^{-2}$ , the values of  $\epsilon_{xx}$  from 0.8% to 1.2% and Sn content from 6.5% to 8.5% present an interesting range that gives a good gain. Figure 7(b) also gives an additional estimated optimum line for 16 nm wide QW, and it does not change much with the QW width from 14 to 16 nm. We can assume the well width varying around 15 nm will not have a large impact on the result of optimum choice of parameters, although it will change the energy that these parameters give because of quantization effects. For the carrier density of  $3 \times 10^{12} \text{ cm}^{-2}$ , the optimum strain is lower (0.7%–0.9%), but the tin content is higher (8.5%–10%). For carrier density lower than  $3 \times 10^{12}$ , it is hard to find a good net gain for photon emission energy higher than 420 meV. However, for photon energies below 420 meV, the available parameter space is effectively limited by limitations in the growth technology. Here we assume the strain to be limited to 1.7%, and if the realistic limit is even lower than that, in order to have higher gain for a given photon energy one should make full use of the available range of strain. If the growth technology permits higher strains, this will provide a better scope for designing GeSn QW lasers with photon energies below 0.42 eV.

#### F. Comparison and analysis

A structure with compressive strain in the well is here compared with a modified tensile-strained structure. Figure 8(a) shows

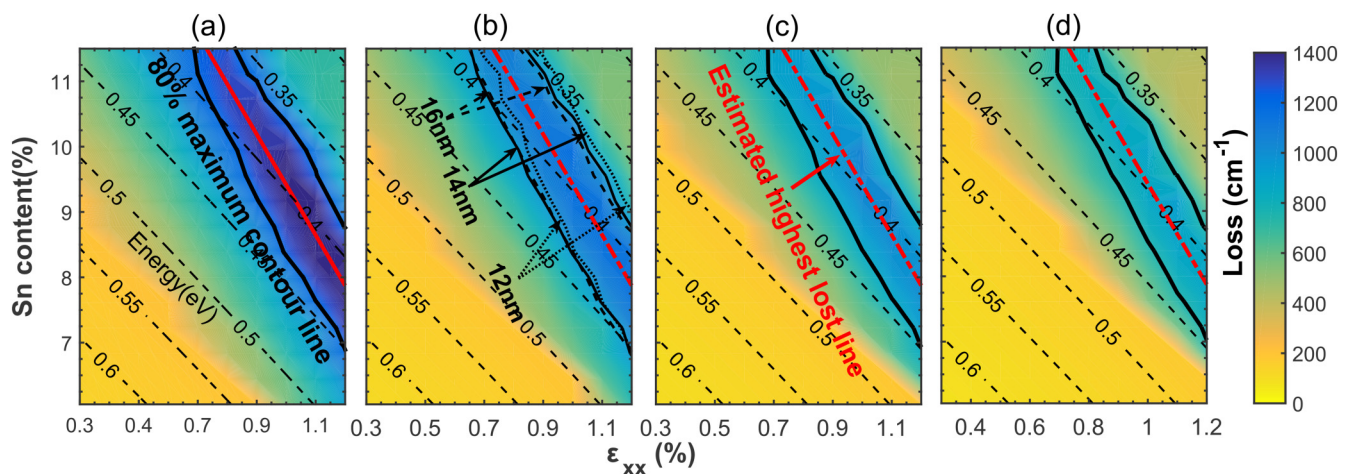


**FIG. 6.** Losses from IVBA and FCA at photon emission energy for (a)  $5 \times 10^{12} \text{ cm}^{-2}$ , (b)  $4 \times 10^{12} \text{ cm}^{-2}$ , (c)  $3.5 \times 10^{12} \text{ cm}^{-2}$ , and (d)  $3 \times 10^{12} \text{ cm}^{-2}$  carrier densities in the structure parameter space. The red line shows the estimate of the highest losses. The solid black contour lines denote the loss of 80% of the maximum. The 80% contour lines for different well widths, for  $4 \times 10^{12} \text{ cm}^{-2}$  carrier density are shown in (b).

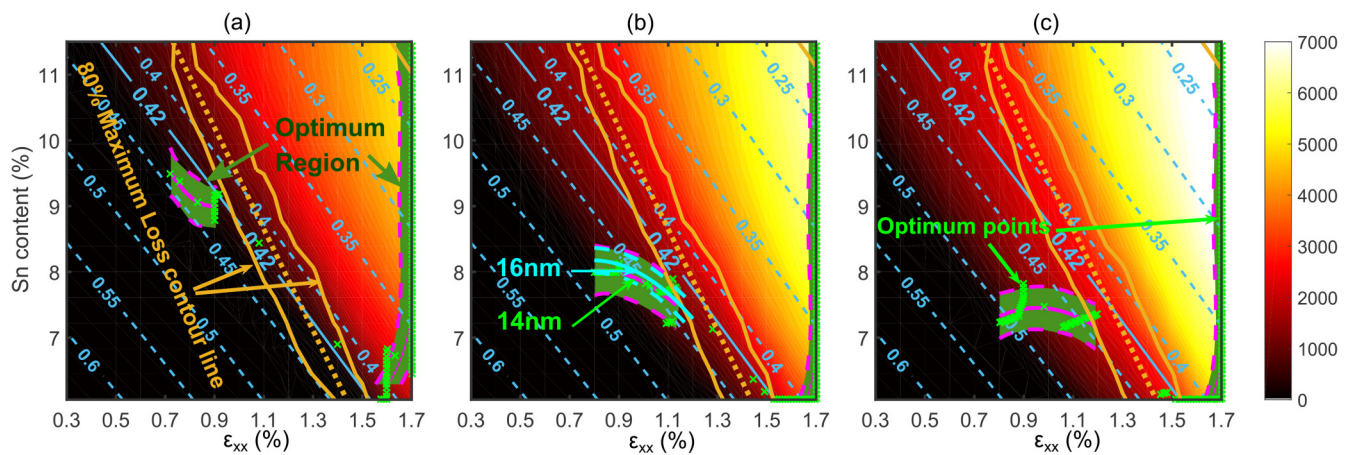


**FIG. 7.** The maximum net gain found in the parameter space of tensile strain and Sn content, for a 14 nm wide QW. The highest gain values for different photon emission energies are denoted by green crosses. The suggested optimum combinations of parameters are shown by the green shadow area. The blue dashed line is the estimated high-loss line. (a)  $3 \times 10^{12} \text{ cm}^{-2}$ , (b)  $4 \times 10^{12} \text{ cm}^{-2}$ , and (c)  $5 \times 10^{12} \text{ cm}^{-2}$ .

a compressively strained MQW structure (sample A).<sup>17</sup> In this work, a SiGeSn/GeSn MQW was grown pseudomorphically on a partially relaxed  $\text{Ge}_{0.916}\text{Sn}_{0.084}$  buffer layer. The Si content is 5% in the barrier, and the Sn contents are 6.3% and 13.8% in the barrier and well layer, respectively. Since the buffer layer of this structure is not fully relaxed, the strain profile used in calculations for this structure was taken from the measurements,<sup>17</sup> so the well layers have compressive in-plane strain of  $\epsilon_{xx} = -1.05\%$ . Figure 9 shows the potential profile of band edges and the quantized subband energy levels for both structures from Fig. 8. The transition energy of the structure in Fig. 8(a) is 0.44 eV (0.45 eV calculated in Ref. 17). Tensile strain can be introduced into GeSn QW by growing the structure on a buffer layer with a larger Sn content. A practical structure has been realized in Ref. 25, but the buffer layer is still partially relaxed. Note that the influence of such a buffer layer with large Sn content on the performance of the device (e.g., via carrier loss, due to band alignment) is not considered in this work (i.e., the buffer layer just acts as the strain provider). Although it seems that the buffer layer will have a small effect, because the collection occurs at the SiGeSn barrier layer which is above the buffer layer,<sup>13</sup> in order to avoid the potential hazards one can use an alternative way to introduce strain, by applying  $\text{SiN}_x$  as the stressor.<sup>54</sup> Here we assume that the buffer layer is fully relaxed

so that the above layers are extended to match the lattice constant of the buffer layer. Figure 8(b) shows the modified structure (sample B), with a 1.25% tensile strain in the well layer (1.67% in the barrier). The strain is introduced by a fully relaxed  $\text{Ge}_{0.85}\text{Sn}_{0.15}$  buffer layer. The thickness of well layers is reduced to 15 nm, according to the predicted optimal choice, from Sec. III B. Inspired by the InGaAsSb MQW laser,<sup>55</sup> the ratio of barrier width/well width is set as 2 (20 nm barrier). Also, the Si content in the barrier is increased to 8% to provide a good carrier confinement factor. Finally, in order to have the same transition energy (0.44 eV) as in Fig. 8(a), a lower Sn content of 6.7% in the well is used. From Fig. 9, we can see that, compared to the compressively strained QW, the difference between the first quantized  $\Gamma$ -valley and L-valley states ( $\Delta E_{\Gamma_1}^{\text{L}}$ ) of the tensile-strained QW has increased from 58 to 78 meV. This leads to the fraction of electrons populating the  $\Gamma$ -valley states to increase from 12.4% to 17.8% for a carrier density of  $5 \times 10^{12} \text{ cm}^{-2}$  at room temperature. Under tensile strain, the LH will be shifted above HH. The difference between the first quantized LH and HH states ( $\Delta E_{\text{HH1}}^{\text{LH1}}$ ) for this tensile-strained QW is 140 meV. In the compressive strain case, the HH ground state will be higher than LH. The SiGeSn/GeSn structure will provide a deep well for HH, and a shallow LH well embedded in it. Although HH1 and LH1 also have a distinct difference of 89 meV for  $-1.05\%$  compressive strain, the wide well width and a large effective mass of HH result in a number of HH subbands near each other (and therefore significantly populated), but higher states do not contribute to the gain peak. The carriers will populate these bands before populating LH1. This effect becomes more important at higher temperatures and will strongly affect the performance of a laser operating at room temperature. However, for tensile strain LH1 becomes the fundamental subband, and a better performance can be expected due to a larger spacing between LH1 and HH1 or higher LH states.

The gain of both structures at 300 K, for different volume carrier densities, is shown in Fig. 10. Since the compressive strained QW only shows the TE mode gain, and tensile-strained QW gives a

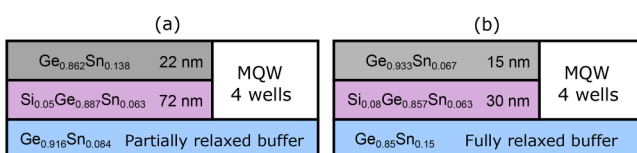


**FIG. 8.** Schematic diagrams of multi-quantum-well structures. (a) Sample A: MQW with  $-1.05\%$  compressive strain in well layers.<sup>17</sup> (b) Sample B: MQW with 1.25% tensile strain in well layers.

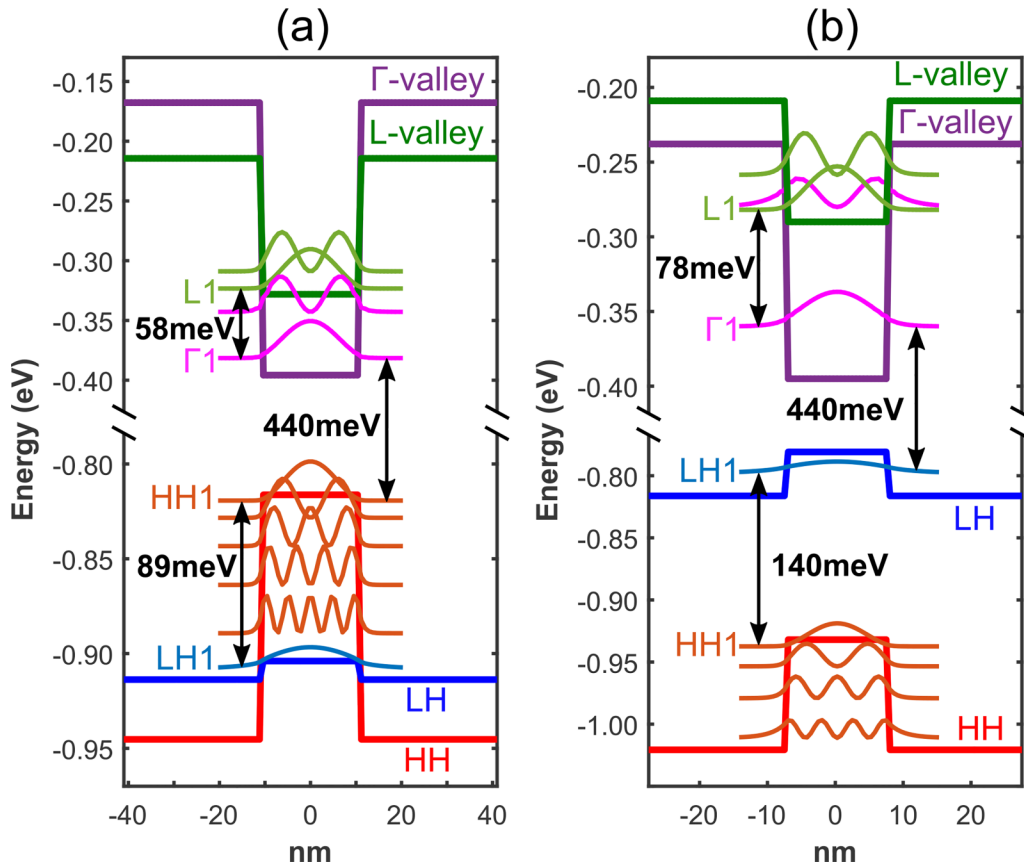


FIG. 9. QW potential profiles of various bands, and the quantized subbands at the center of Brillouin zone and at the L-valley, for (a) sample A and (b) sample B.

much higher TM than TE mode gain, only the major polarization is shown in this figure. From Figs. 10(a)–10(c), it is clear that sample B gives a much higher inter-band gain. This is expected because larger  $\Delta E_{\Gamma 1}^{L1}$  and  $\Delta E_{HH1}^{LH1}$  are indeed found here. The net gain is obtained by considering the loss from IVBA and FCA. As can be seen in Fig. 10, the tensile-strained structure has a better performance because of its higher inter-band gain, but it also has a much larger IVBA. The IVBA appears to be a major potential hazard when designing a tensile-strained QW. Nevertheless, the proposed SiGeSn/GeSn tensile-strained structure even has a comparable gain with that of the AlGaAs/GaAs structure. The TE gain peaks of Al<sub>0.45</sub>Ga<sub>0.55</sub>As (12 nm)/GaAs (8 nm) MQW<sup>56</sup> for the same carrier density are denoted in Fig. 10(d). They amount to 237, 817, and 1306 cm<sup>-1</sup> at ~1.59 eV, compared with 221, 999, and 1614 cm<sup>-1</sup> at ~0.44 eV for GeSn QW. Although the GaAs QW has a directness of ~280 meV, which is much higher than the tensile-strained GeSn QW (78 meV), the proposed SiGeSn/GeSn QW still has slightly higher gain, because the strain significantly shifted up the LH states, reducing the density of states at the valence band top.

We now combine sample B with an electrically pumped laser design<sup>20</sup> to get a rough estimate of its performance. In Fig. 11(a), a

silica ridge (2  $\mu$ m wide) with lower refractive index is used to provide a better optical confinement. The MQW structure is sandwiched between two n/p-doped Si<sub>0.08</sub>Ge<sub>0.853</sub>Sn<sub>0.067</sub> layers. The whole structure is grown on the Ge<sub>0.85</sub>Sn<sub>0.15</sub> buffer layer to introduce strain into the well layer. The relationship between carrier density and current density is calculated from

$$J_{tot} = \frac{qL_{active}}{\sigma_{inj}} (\mathcal{A}_{nr}N_v + \mathcal{R}_{\Gamma}P_vN_v\Theta_{\Gamma} + \mathcal{R}_{L}P_vN_v\Theta_{L} + C_nN_v^2P_v + C_pN_vP_v^2), \quad (25)$$

in which  $J_{tot}$  is the current density,  $q$  is the electron charge,  $L_{active}$  is the active region width,  $\sigma_{inj}$  is the injection efficiency,  $\mathcal{A}_{nr}$  is the nonradiative recombination rate,  $\mathcal{R}_{\Gamma}$  and  $\mathcal{R}_{L}$  are the recombination coefficients for  $\Gamma$  and L valleys, and  $\Theta_{\Gamma}$  and  $\Theta_{L}$  are the fractions of the electron population in the  $\Gamma$ - and L-valleys.  $N_v$  and  $P_v$  are 3D (volume) carrier densities of electrons and holes, and  $C_n$  and  $C_p$  are the electron and hole Auger recombination rates. The threshold current density is evaluated when modal gain (= net gain  $\times$  optical confinement factor) is equal to the sum of the intrinsic modal loss

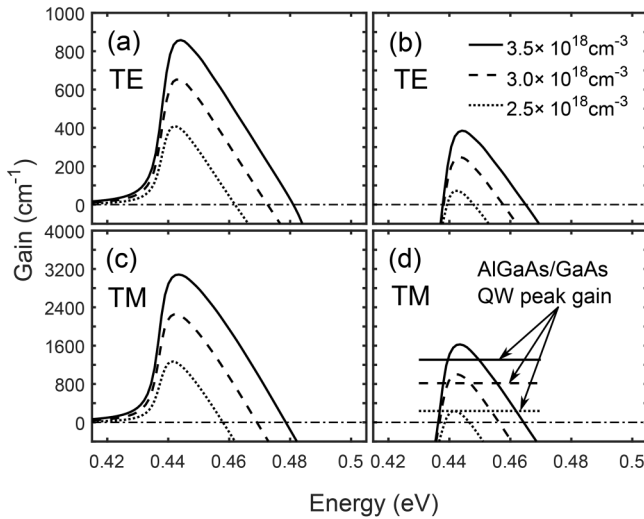


**FIG. 10.** Inter-band gain and net gain for carrier densities from  $2.5 \times 10^{18}$  to  $3.5 \times 10^{18} \text{ cm}^{-3}$  at room temperature: (a) TE inter-band gain of sample A compressively strained QW, (b) TE net gain of sample A, (c) TM inter-band gain of sample B tensile-strained QW, and (d) TM net gain of sample B.

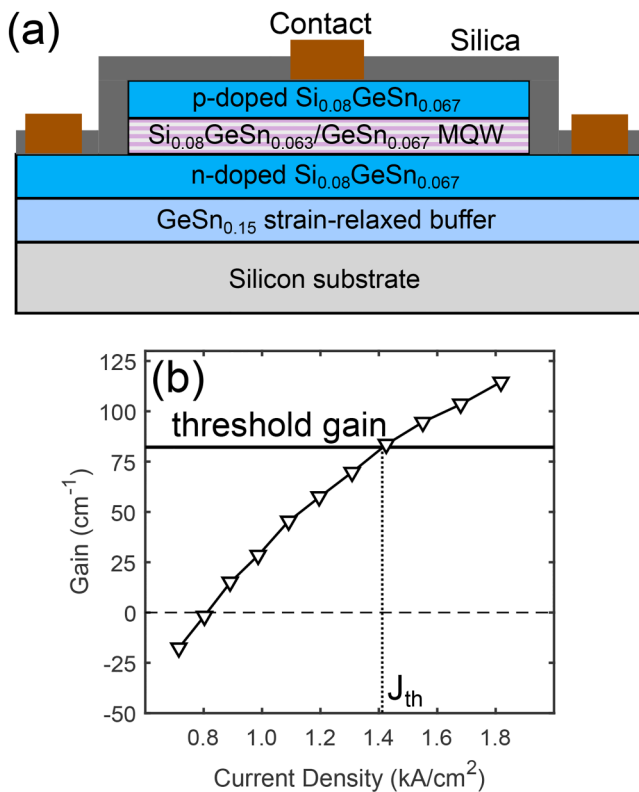


**FIG. 11.** (a) Schematic diagram of an electrically pumped laser. In the active region, the (Si)Sn content and widths of the barrier layers and well layers are the same as in sample B. (b) The estimated model gain vs the current density.

and mirror loss. The modal loss and mirror loss were chosen according to the modeling results of Ref. 20 (modal loss + mirror loss =  $82.16 \text{ cm}^{-1}$ ). The optical confinement factor is set to 6.98%.<sup>20</sup> As for the recombination coefficients, we have taken their values in Ge, shown in Table V. Figure 11(b) shows the modal gain vs current density calculated with these parameters. A threshold current of  $1.415 \text{ kA/cm}^2$  was found if the injection efficiency is 0.75. This can be compared with some results typical for AlGaAs/GaAs MQW structures (e.g., in Ref. 57  $1.05\text{--}1.2 \text{ kA/cm}^2$  for an  $\text{Al}_{0.09}\text{Ga}_{0.91}\text{As/GaAs}$  10 MQW and in Ref. 58  $4.2 \text{ kA/cm}^2$  for an  $\text{Al}_{0.3}\text{Ga}_{0.7}\text{As/GaAs}$  10 MQW in continuous wave operation).

We further give some more information about the optimization based on sample B. By changing the Sn content in the well and modifying the strain by adjusting the Sn mole fraction in the buffer layer, several designs with the same photon emission energy can be achieved. From Fig. 12(a), although a larger strain reduces the required Sn content in the well layer, an increased Sn fraction in the buffer layer is needed. This will bring about difficulties in fabrication technology, and the larger strain will also give some restrictions regarding the critical thickness. Higher strain, but lower Sn content, will bring about two effects: (1) a larger difference between LH1 and HH1, as indicated by  $\Delta E_{HH1}^{LH1}$  in Fig. 12(b), which is good for gain, and (2) it will also give a smaller directness because  $\Delta E_{\Gamma_1}^{L_1}$  decreases with increasing  $\epsilon_{xx}$ , and this is unfavorable for performance. A larger difference in LH and HH energies will not provide a significant improvement if this difference is already large. For example,  $\Delta E_{HH1}^{LH1}$  is 169.7 meV for a 1.5% strain (compared to  $6k_bT = 155.1 \text{ meV}$  at 300 K), but at the same time the change in  $\Delta E_{\Gamma_1}^{L_1}$  could play a more important role when increasing the strain. For a lower carrier density, the highest point of inter-band gain peak is found for  $\epsilon_{xx} = 1.5\%$ . This comes as the result of two opposite effects. For higher carrier density [in Fig. 12(d)], the curve is monotonic as the Fermi level becomes deeper and the difference between LH and HH becomes the most important effect in the parameter space. It is also worth mentioning that a loss peak is found at 1.45% tensile strain in Figs. 12(c) and 12(d), which implies the “loss ridge” mentioned in Sec. III D. Note that by combining the trends of the inter-band gain peak and the loss, a possible local optimal choice for lower strain can be found at a certain carrier density. For example, in Fig. 12(c), when  $\epsilon_{xx} = 1.25\%$  (sample B), the net gain is highest for  $\epsilon_{xx}$  from 0.9% to 1.45%, indicating a possible lower threshold for a design with lower strain in the well.

**TABLE V.** Recombination coefficients in Ge.

Material	$\mathcal{A}_{nr}(\text{s}^{-1})$	$\mathcal{R}_\Gamma(\text{cm}^{-3} \text{ s}^{-1})$	$\mathcal{R}_L(\text{cm}^{-3} \text{ s}^{-1})$	$C_n(\text{cm}^{-6} \text{ s}^{-1})$	$C_p(\text{cm}^{-6} \text{ s}^{-1})$
Ge	$10^{-6a}$	$1.3 \times 10^{-10b}$	$5.1 \times 10^{-15b}$	$2.2 \times 10^{-30c}$	$5.4 \times 10^{-31c}$

<sup>a</sup>Reference 20.

<sup>b</sup>Reference 59.

<sup>c</sup>Reference 60.

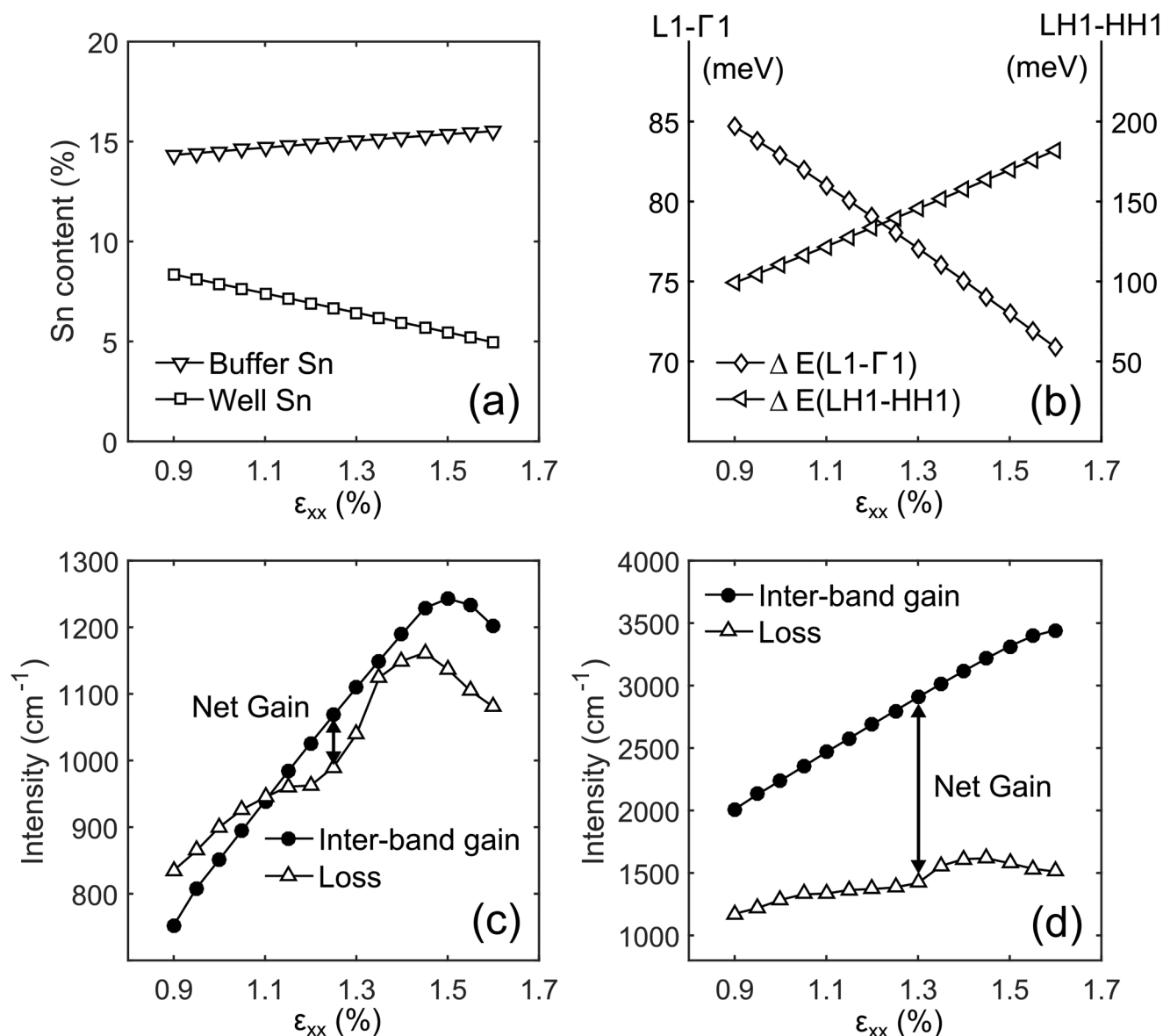


**FIG. 12.** (a) Parameters for a 15 nm GeSn QW wrapped by  $\text{Si}_{0.08}\text{Ge}_{0.857}\text{Sn}_{0.063}$  barrier, required to produce a transition energy of 0.44 eV, by varying the in-plane tensile strain, Sn content in the well to provide the same transition energy and Sn content in the GeSn buffer layer to have the corresponding strain. (b) Energy spacing between the first quantized states of L-valley and  $\Gamma$ -valley and between LH and HH states. (c) For  $3.6 \times 10^{12} \text{ cm}^{-2}$  and (d)  $5 \times 10^{12} \text{ cm}^{-2}$  2D carrier density, the inter-band peak gain and loss at this peak coming from IVBA and FCA at 300 K [we used the corresponding Sn fractions in the well and buffer in (a) to calculate the results of (b)–(d)].

### G. Carrier density and doping

The relationship between the quasi-Fermi level and the carrier density for two different structures is illustrated in Fig. 13. Structure with indirect bandgap needs a larger injected carrier density, or doping, to reach population inversion. For an indirect bandgap material like germanium, n-type doping is often used.<sup>61</sup> In Fig. 13(a), a near-indirect material is used, the L-valley and

$\Gamma$ -valley have similar band edges, but the bandgap is still indirect. Since more carriers will populate the L valley, it is harder for the electron Fermi level to reach the  $\Gamma$ -valley minimum. It is then reasonable to choose n-doping, rather than p-doping, to improve the gain.

Figures 14(a) and 15(a) show gain spectra of the two structures in Fig. 13 for different injected carrier densities, in case of no

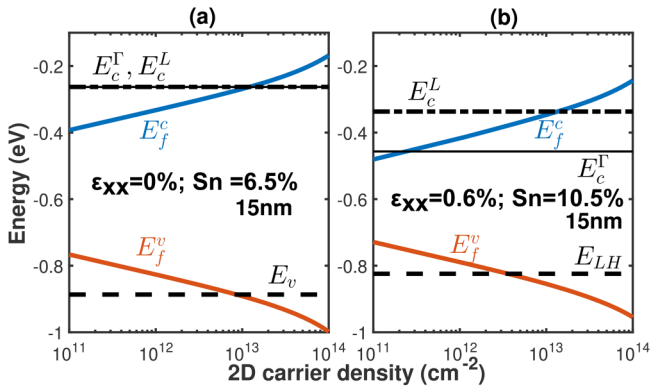


**FIG. 13.** Quasi-Fermi level vs 2D carrier density of two 15 nm SiGeSn/GeSn QWs. (a) Indirect well layer, Sn content = 6.5%,  $\epsilon_{xx} = 0\%$  (b) Direct well layer, Sn content = 10.5%,  $\epsilon_{xx} = 0.6\%$ .

doping. Figure 14(b) [Fig. 15(b)] and Fig. 14(c) [Fig. 15(c)] are the gain spectra for the same doping density but with different doping types. The black dashed lines in Fig. 14 (also in Fig. 15) indicate the energy difference between the first CB and (LH)HH at the center of the Brillouin zone. In Fig. 14, the first CB and HH states contribute to the TE mode gain, and the first LH band starts to contribute to the TE mode gain when doping, together with carrier density, is large enough. The spectra then feature a curve with a double peak near  $E_{hh1}^{e1}(0)$  and  $E_{lh1}^{e1}(0)$ . For the TM mode, heavy holes do not give any contribution to gain. The TM peaks are then located near  $E_{lh1}^{e1}(0)$ . We can see that, although both p- and n-doping can be used to achieve gain, the general performance of n-doping is significantly better than that of p-doping, especially for the first peak of the TE mode near  $E_{hh1}^{e1}(0)$ . However, this is not

always the case. We find that p-doping may be useful when the band structure is direct. Figure 15 considers a direct bandgap structure. In such (or similar) structure, because of high strain and Sn content,  $\Gamma$ -valley is much lower than L-valley, the conduction band can be well populated with electrons while the top valence band, which has a flatter dispersion, will have the holes distributed over a wider range of  $k$ -vectors. The p-doping may be useful in such a situation. As shown in Fig. 15, the TM mode is most important in such cases. LH1 has replaced HH1 as the first valence subband. So, the first peak of the TE and TM mode gain appears at  $E_{lh1}^{e1}(0)$ . The second peak can be observed for TE mode for high carrier density, at  $E_{hh1}^{e1}(0)$ . But this is far from the first peak and less important. In contrast to Fig. 14, the gain spectrum for p-doping has a larger peak. The largest difference in this test appears when injected carrier density is  $5 \times 10^{12} \text{ cm}^{-2}$ , the peak gain for  $2 \times 10^{12}$  p-doping is 19.24% higher than for  $2 \times 10^{12}$  n-doping, indicating that p-doping will deliver a better performance in such or similar circumstances.

As shown in Fig. 13, in both cases, the  $E_{fc}$  and  $E_{fv}$  lines are essentially symmetric, which means that the variation of electron and hole quasi-Fermi levels is similar for the same amount of n- and p-doping. Therefore, for carrier density in the range  $10^{12}$ – $10^{14} \text{ cm}^{-2}$ , the same amount of n- and p-type doping will bring about the same change in quasi-Fermi level ( $\Delta E_{fc}/\Delta N = \Delta E_{fv}/\Delta P$ ). In Fig. 16, the Fermi functions for n-doping and p-doping in the same reference system are shown separately on the left and right. It is clear that for the transition energy  $\hbar\omega$ , the absolute value of Fermi–Dirac inversion factor for p-type doping is larger than for n-type doping. This is because of the original quasi-Fermi level, the absolute value of derivative of the conduction band Fermi–Dirac function  $|(df_c/dE)|_{E_i(k)}$  will be smaller than derivative of the valence band Fermi–Dirac function  $|(df_v/dE)|_{E_i(k)} = |(df_v/dE_{fv})|_{E_i(k)}$  because of a smaller density of states in the

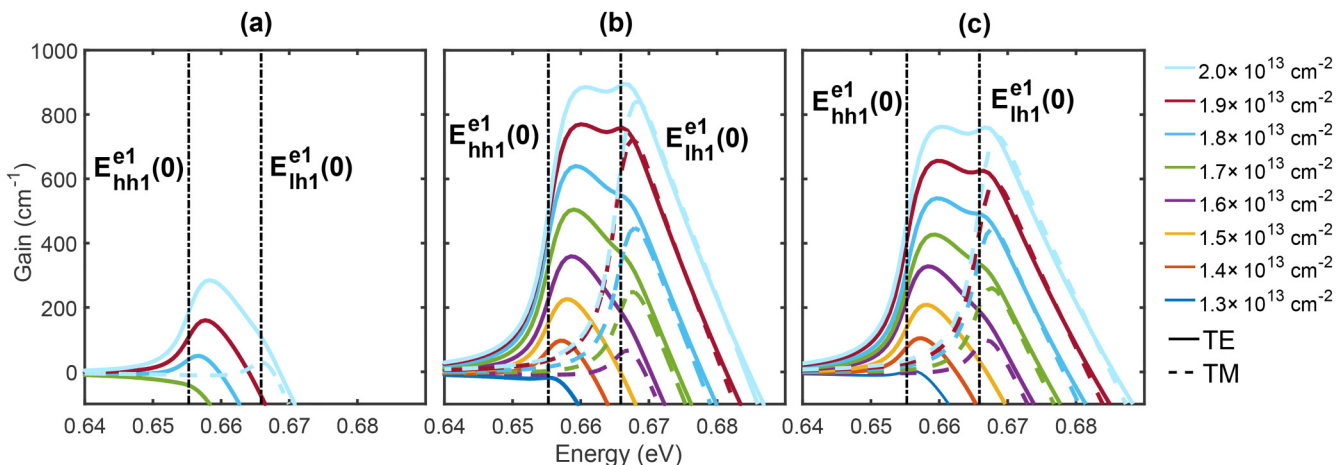


**FIG. 14.** Gain spectra of 15 nm wide SiGeSn/GeSn QW, with Sn content = 6.5% and  $\epsilon_{xx} = 0\%$ , for carrier densities from  $1.3 \times 10^{13}$  to  $2.0 \times 10^{13} \text{ cm}^{-2}$ : (a) no doping, (b) n-doping =  $1 \times 10^{13} \text{ cm}^{-2}$ , and (c) p-doping =  $1 \times 10^{13} \text{ cm}^{-2}$ .

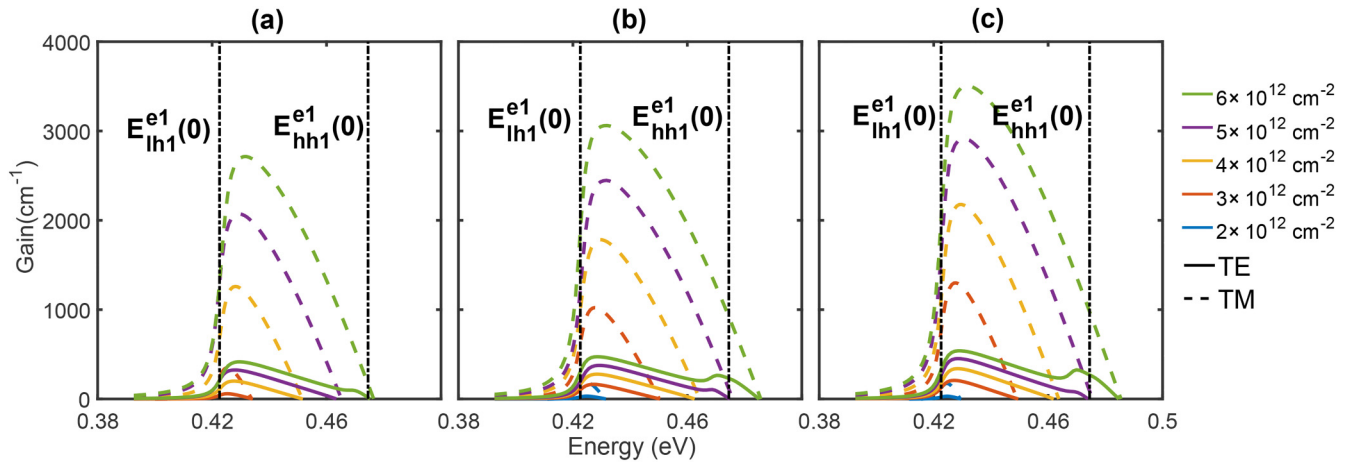


**FIG. 15.** Gain spectra of 15 nm wide SiGeSn/GeSn QW, with Sn content = 10.5% and  $\epsilon_{xx} = 0.6\%$  for carrier densities from  $2 \times 10^{12}$  to  $6 \times 10^{12} \text{ cm}^{-2}$ : (a) no doping, (b) n-doping =  $2 \times 10^{12} \text{ cm}^{-2}$ , and (c) p-doping =  $2 \times 10^{12} \text{ cm}^{-2}$ .

conduction band. So, when the quasi-Fermi level is more “biased” toward the conduction band, p-doping will give a larger Fermi–Dirac inversion factor and a larger gain will be observed. Furthermore, we can conclude that if  $\Delta E_{fc}/\Delta N \cong \Delta E_{fv}/\Delta P$  is fulfilled, in order to make the full use of doping for a QW, if  $E_{fc} + E_{fv} > E_c^1 + E_v^1$  the p-doping is preferable, and when  $E_{fc} + E_{fv} < E_c^1 + E_v^1$  the n-doping is preferable. For a bulk material,  $E_c^1$  and  $E_v^1$  can be replaced by band edge energy of the conduction band and the valence band. This rule can be applied at any temperature, and at high temperatures (e.g., 300 K) the effect of doping and carrier density will be gradual, so a proper doping can still help to improve the performance when both  $E_{fc} > E_c^1$  and  $E_{fv} < E_v^1$  are fulfilled. However, at low temperatures, the behavior of gain under different doping and carrier densities will be more “step-like,” and if  $E_{fc} > E_c^1$  and  $E_{fv} < E_v^1$  can be achieved with a given injected carrier density, the gain improvement by doping will be very limited. A simple physical

explanation of the gain improvement by p-doping in strongly direct band structure cases is related to a large mismatch of effective masses between the conduction band and the valence band. With much larger mass, the holes will be thermally distributed over a wider range of in-plane k-vectors than electrons, and only a small fraction of holes will contribute to gain. This can be compensated by adding more holes in the system. Of course, the free carrier absorption would also increase for too large p-doping, but for a limited p-doping the net gain will improve. The benefits of p-doping have previously been discussed for MQWs based on other materials, e.g., in Ref. 62.

#### IV. CONCLUSION

Gain calculations for SiGeSn/GeSn QWs show that the well width of 13–16 nm is a good choice to get the high TM mode gain. The transition energy is mainly determined by the Sn content and tensile strain. At higher photon emission energies, good gain can be obtained with different combinations of Sn content and strain, also depending on the carrier density, but for low photon emission energy the optimal design is restricted by the limits of the available parameter space. The well width can also influence the transition energy, but it will only vary about 25 meV for widths between 13 and 16 nm. For a particular transition energy, using higher Sn content and lower strain will make the bandgap more direct, while using higher strain and lower Sn content will give a less direct bandgap but will also make the topmost valence band quantized state more separated from other states. To explore the trade-offs involved, the optimum choices are found by calculating gain for various structures in the practically interesting range of parameters ( $\epsilon_{xx} = 0.3\% - 1.7\%$ , Sn = 6.056%–11.5%), and by finding the highest gain for a chosen energy by interpolation. IVBA and FCA are very important in the design of SiGeSn/GeSn lasers, as these losses are very significant between 0.35 and 0.45 eV. The region in parameter space where the highest losses occur at photon emission energy does not vary much, and the optimum region should avoid

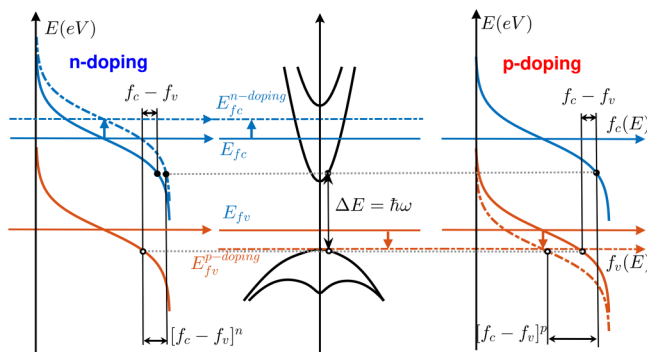


**FIG. 16.** Schematic diagram showing how n-doping and p-doping affect the Fermi–Dirac inversion factor for optical transitions at  $\hbar\omega$ . It is clear that for  $E_{fc} + E_{fv} > E_c + E_v$ , the p-doping gives a higher inversion factor than n-doping.

this high-loss area. Because of that, we found that the optimum region for photon energy higher than 0.42 eV may depend on the injected carrier densities. However, for photon energy less than 0.42 eV, the lowest Sn content is always preferable because we assumed 1.7% tensile strain as the technological limit. A broader space for the design of optimal GeSn QWs with low photon emission energy would appear only if higher tensile strain becomes available by appropriate technology development.

Doping can help to improve the performance if the correct type of doping is chosen. N-doping was often used in Ge and other indirect bandgap materials. In this work, we find that p-doping may be a better choice than n-doping to improve the performance of the direct bandgap SiGeSn/GeSn QW structure. A general rule that p-doping is preferable when  $E_{fc} + E_{fv} > E_c + E_v$ , while n-doping is better when  $E_{fc} + E_{fv} < E_c + E_v$ , can also be extended to other materials or structures like QWs.

## APPENDIX: HAMILTONIAN AND MOMENTUM MATRIX ELEMENTS

The spin-orbit part of the Hamiltonian was given incorrectly in Ref. 31. Equation (11) is from the erratum of this paper.<sup>63</sup>

Non-zero parts of momentum matrix elements used to calculate the absorption are

For TE polarization:

$$\sum_{ij} \langle F_{s,i}(z, \mathbf{k}_{\parallel}) | F_{t,i}(z, \mathbf{k}_{\parallel}) \rangle \langle u_i | \hat{\mathbf{p}}_x | u_j \rangle = -\frac{m_0 P_0}{\hbar} \left( -\frac{1}{\sqrt{6}} \langle F_{s,1} | F_{t,3} \rangle - \frac{1}{\sqrt{6}} \langle F_{s,3} | F_{t,1} \rangle - \frac{1}{\sqrt{2}} \langle F_{s,1} | F_{t,5} \rangle - \frac{1}{\sqrt{2}} \langle F_{s,5} | F_{t,1} \rangle - \frac{1}{\sqrt{3}} \langle F_{s,1} | F_{t,8} \rangle - \frac{1}{\sqrt{3}} \langle F_{s,8} | F_{t,1} \rangle + \frac{1}{\sqrt{2}} \langle F_{s,2} | F_{t,4} \rangle + \frac{1}{\sqrt{2}} \langle F_{s,4} | F_{t,2} \rangle + \frac{1}{\sqrt{6}} \langle F_{s,2} | F_{t,6} \rangle + \frac{1}{\sqrt{6}} \langle F_{s,6} | F_{t,2} \rangle - \frac{1}{\sqrt{3}} \langle F_{s,2} | F_{t,7} \rangle - \frac{1}{\sqrt{3}} \langle F_{s,7} | F_{t,2} \rangle \right). \quad (26)$$

For TE polarization:

$$\sum_{ij} \langle F_{s,i}(z, \mathbf{k}_{\parallel}) | F_{t,i}(z, \mathbf{k}_{\parallel}) \rangle \langle u_i | \hat{\mathbf{p}}_z | u_j \rangle = -\frac{m_0 P_0}{\hbar} \left( \sqrt{\frac{2}{3}} \langle F_{s,1} | F_{t,6} \rangle + \sqrt{\frac{2}{3}} \langle F_{s,6} | F_{t,1} \rangle + \frac{1}{\sqrt{3}} \langle F_{s,1} | F_{t,7} \rangle + \frac{1}{\sqrt{3}} \langle F_{s,7} | F_{t,1} \rangle + \sqrt{\frac{2}{3}} \langle F_{s,2} | F_{t,3} \rangle + \sqrt{\frac{2}{3}} \langle F_{s,3} | F_{t,2} \rangle - \frac{1}{\sqrt{3}} \langle F_{s,2} | F_{t,8} \rangle - \frac{1}{\sqrt{3}} \langle F_{s,8} | F_{t,2} \rangle \right). \quad (27)$$

## DATA AVAILABILITY

The data that support the findings of this study are available from the corresponding authors upon reasonable request

## REFERENCES

- <sup>1</sup>M. P. Polak, P. Scharoch, and R. Kudrawiec, *J. Phys. D: Appl. Phys.* **50**, 195103 (2017).
- <sup>2</sup>S. Gupta, B. Magyari-Köpe, Y. Nishi, and K. C. Saraswat, *J. Appl. Phys.* **113**, 073707 (2013).
- <sup>3</sup>S. Wirths *et al.*, *Nat. Photonics* **9**, 88 (2015).
- <sup>4</sup>Q. M. Thai *et al.*, *Opt. Express* **26**, 32500 (2018).
- <sup>5</sup>Y. Zhou *et al.*, *Optica* **7**(8), 924–928 (2020).
- <sup>6</sup>A. Attiaoui and O. Moutanabbir, *J. Appl. Phys.* **116**, 063712 (2014).
- <sup>7</sup>D. Rainko *et al.*, *Sci. Rep.* **8**, 15557 (2018).
- <sup>8</sup>A. Elbaz *et al.*, *Nat. Photonics* **14**, 375–382 (2020).
- <sup>9</sup>N. von den Driesch *et al.*, *Small* **13**, 1603321–1603330 (2017).
- <sup>10</sup>D. Stange *et al.*, *Optica* **4**, 185–188 (2017).
- <sup>11</sup>S. A. Ghetmiri *et al.*, *Opt. Lett.* **42**, 387–390 (2017).
- <sup>12</sup>W. Du *et al.*, *J. Appl. Phys.* **122**, 123102 (2017).
- <sup>13</sup>G. Abernathy *et al.*, *arXiv:2009.12254* (2020).
- <sup>14</sup>D. Stange *et al.*, *ACS Photonics* **5**, 4628–4636 (2018).
- <sup>15</sup>P. C. Grant *et al.*, *AIP Adv.* **8**, 025104 (2018).
- <sup>16</sup>P. C. Grant *et al.*, *Nanotechnology* **29**, 465201 (2018).

- <sup>17</sup>J. Margetis *et al.*, *Appl. Phys. Lett.* **113**, 221104 (2018).
- <sup>18</sup>Y. Zhou *et al.*, in *Conference on Lasers and Electro-Optics*, OSA Technical Digest (Optical Society of America, 2019), paper STu3N.3.
- <sup>19</sup>Y. -H. Zhu *et al.*, *J. Appl. Phys.* **107**, 073108 (2010).
- <sup>20</sup>G. -E. Chang *et al.*, *IEEE J. Quantum Electron.* **46**(12), 1813–1820 (2010).
- <sup>21</sup>H. S. Mączko *et al.*, *Sci. Rep.* **6**, 34082 (2016).
- <sup>22</sup>Y. Liu *et al.*, *IEEE Photonics J.* **10**(1), 1500609 (2018).
- <sup>23</sup>Q. M. Thai *et al.*, *Phys. Rev. B* **102**, 155203 (2020).
- <sup>24</sup>D. Peschka *et al.*, *IEEE Photonics J.* **7**, 1 (2015).
- <sup>25</sup>S. Wirths *et al.*, *Appl. Phys. Lett.* **103**, 192110 (2013).
- <sup>26</sup>M. Morea *et al.*, in *IEEE Photonics Society Summer Topical Meeting Series (SUM)* (Institute of Electrical and Electronics Engineers, 2016), pp. 21–22.
- <sup>27</sup>Q. Zhang, Y. Liu, J. Yan, C. Zhang, Y. Hao, and G. Han, *Opt. Express* **23**, 7924 (2015).
- <sup>28</sup>R. Kuroyanagi, L. M. Nguyen, T. Tsuchizawa, Y. Ishikawa, K. Yamada, and K. Wada, *Opt. Express* **21**, 18553 (2013).
- <sup>29</sup>J. Chrétien *et al.*, *ACS Photonics* **6**, 2462 (2019).
- <sup>30</sup>C. Eckhardt *et al.*, *Phys. Rev. B* **89**, 165201 (2014).
- <sup>31</sup>C. Xu *et al.*, *Chem. Mater* **31**(23), 9831–9842 (2019).
- <sup>32</sup>B. Cao *et al.*, *ACS Appl. Mater. Interfaces* **12**, 57245–57253 (2020).
- <sup>33</sup>Z. Song *et al.*, *New J. Phys.* **22**, 019502 (2020).
- <sup>34</sup>E. O. Kane, *J. Phys. Chem. Solids* **1**, 249 (1957).
- <sup>35</sup>G. L. Bir and G. E. Pikus, *Symmetry and Strain-Induced Effects in Semiconductors* (Wiley, New York, 1974).

- <sup>36</sup>T. B. Bahder, *Phys. Rev. B* **41**, 11992 (1990).
- <sup>37</sup>S. Birner, Ph.D. thesis, TMU, 2011.
- <sup>38</sup>J. M. Luttinger, *Phys. Rev.* **102**, 1030 (1956).
- <sup>39</sup>B. A. Foreman, *Phys. Rev. B* **56**, R12748 (1997).
- <sup>40</sup>E. Anderson *et al.*, *LAPACK Users' Guide*, 3rd ed. (Society for Industrial and Applied Mathematics, Philadelphia, PA, 1999).
- <sup>41</sup>A. Rahman, M. S. Lundstrom, and A. W. Ghosh, *J. Appl. Phys.* **97**, 053702 (2005).
- <sup>42</sup>R. Winkler, *J. Phys.: Condens. Matter* **5**, 2321 (1993).
- <sup>43</sup>J. Liu *et al.*, *Opt. Express* **15**, 11272 (2007).
- <sup>44</sup>Y.-H. Li *et al.*, *Appl. Phys. Lett.* **94**, 212109 (2009).
- <sup>45</sup>S. Adachi, *Properties of Group IV, III-V and II-VI Semiconductors* (Wiley, New York, 2009).
- <sup>46</sup>H. H. Li, *J. Phys. Chem. Ref. Data* **9**, 561 (1993).
- <sup>47</sup>A. I. Golovashkin and G. P. Motulevich, *Sov. Phys. JETP* **19**, 310 (1964), [http://jetp.ac.ru/cgi-bin/dn/e\\_019\\_02\\_0310.pdf](http://jetp.ac.ru/cgi-bin/dn/e_019_02_0310.pdf).
- <sup>48</sup>S.-Q. Liu and S.-T. Yen, *J. Appl. Phys.* **125**, 245701 (2019).
- <sup>49</sup>D. J. Paul, *J. Appl. Phys.* **120**, 043103 (2016).
- <sup>50</sup>J. Toole *et al.*, *Appl. Phys. Lett.* **89**, 231924 (2006).
- <sup>51</sup>P. Moontragoon *et al.*, *Semicond. Sci. Technol.* **22**, 742 (2007).
- <sup>52</sup>J. D. Gallagher *et al.*, *Appl. Phys. Lett.* **103**, 202104 (2013).
- <sup>53</sup>M. Asada *et al.*, *IEEE J. Quantum Electron.* **17**, 611 (1981).
- <sup>54</sup>C. S. Fenrich *et al.*, *ACS Photonics* **3**(12), 2231–2236 (2016).
- <sup>55</sup>H. Lee *et al.*, *Appl. Phys. Lett.* **66**, 1942 (1995).
- <sup>56</sup>A. Furuya *et al.*, *Jpn. J. Appl. Phys.* **26**, L134 (1987).
- <sup>57</sup>G. Weimann and W. Schlapp, *Physica B + C* **129**(1–3), 459–464 (1985).
- <sup>58</sup>T. Egawa *et al.*, *IEEE Photon. Technol. Lett.* **9**(7), 872–874 (1997).
- <sup>59</sup>J. R. Jian *et al.*, *Nat. Photonics* **6**, 398–405 (2012).
- <sup>60</sup>J. van der Heide *et al.*, *Sol. Energy Mater. Sol. Cells* **93**, 1810 (2009).
- <sup>61</sup>X. Sun *et al.*, *IEEE J. Select. Topics Quantum Electron.* **16**, 124 (2010).
- <sup>62</sup>G. Belenky *et al.*, *IEEE Photon. Technol. Lett.* **12**, 969 (2000).
- <sup>63</sup>T. B. Bahder, *Phys. Rev. B* **46**, 9913 (1992).